

# Contents

<b>1</b>	<b>Introduction</b>	<b>3</b>
1.1	Properties of TMDCs . . . . .	3
1.2	Electronic properties . . . . .	4
1.3	Optical properties . . . . .	6
1.4	Phonon dispersion . . . . .	10
<b>2</b>	<b>Role of precursors in growth of monolayer <math>WS_2</math></b>	<b>12</b>
2.1	Introduction . . . . .	12
2.2	Results . . . . .	13
2.3	Conclusions . . . . .	27
<b>3</b>	<b>WSe<sub>2</sub></b>	<b>29</b>
3.1	Introduction . . . . .	29
3.2	Results . . . . .	29
<b>4</b>	<b>Transfer</b>	<b>36</b>
4.1	Introduction . . . . .	36
4.2	Experimental . . . . .	36
4.3	Results . . . . .	36
4.4	Conclusions . . . . .	38
<b>5</b>	<b>Low T PL</b>	<b>42</b>
5.1	Introduction . . . . .	42
5.2	Experimental . . . . .	42
5.3	Results . . . . .	42
<b>6</b>	<b>1T' <math>WSe_2</math></b>	<b>46</b>
6.1	Introduction . . . . .	46
<b>7</b>	<b>TMDC phases - review</b>	<b>47</b>
7.1	Introduction . . . . .	47
<b>8</b>	<b>Conclusions</b>	<b>48</b>
	<b>References</b>	<b>48</b>

# Physical Characterization of Atomically-Thin Transition Metal Dichalcogenides

Paweł Palczyński

April 1, 2019

## **Declaration**

## **Acknowledgements**

## **Abstract**

## **List of abbreviations**

## **List of figures**

## **List of tables**

# 1 Introduction

Following the discovery and characterisation of graphene in last decade the focus has been put on other 2D materials. Similar to graphene other bulk layered materials can exist in a monolayer or few layer form. Furthermore these thin layers also exhibit a significant change of properties when number of layers decreases from bulk all the way to monolayer. One of the most popular groups of these materials are transition metal dichalcogenides (TMDC). Their general form is  $MX_2$  where M is a transition metal, and X is a chalcogen atom.

## 1.1 Properties of TMDCs

TMDCs in their layered form have been known, studied and utilised for a long time. They can be found commonly in use as stolid-state lubricants or catalysts. About 60 different TMDCs have been studied and characterised with a general formula of X-M-X where a plane of metal atoms (M) is sandwiched between two chalcogen planes (X). Out of those 40 can be considered layered materials where individual layers are strongly bonded in-plane and weakly bonded out-of-plane in between layers. These weak, interlayer, Van der Waals interactions allow to form a bulk material. These bonds are also what allows for those layers to slide on top of one another similarly to other layered materials like graphite. TMDCs consist of two transition metal and single chalcogen atoms covalently bonded. They can be found in 3 distinct structural polytypes: 1T (tetragonal symmetry, octahedral coordination) with single layer per repeat unit, 2H (hexagonal symmetry, trigonal prismatic coordination) with 2 layers per repeat unit and 3R (rhombohedral symmetry, trigonal prismatic coordination) with 3 layers per repeat unit [52] as can be seen in Figure 1.

Since graphene have proven to be difficult to work with in the fields of semiconductors due to its lack of natural finite electronic band gap its role as a successor in electronic and opto-electronic devices remains to be seen. However the techniques learned and effects observed during its characterisation were easily transferred to other layered compounds such as TMDCs. In particular the semiconducting, group VI-based TMDCs, containing sulphur and selenium as chalcogen atoms have proven to be more readily potentially useful as an active material in electronic and opto-electronic devices. This is due to their inherent electronic and optical bandgap in visible-near IR range.

As the number of layers changes from bulk to monolayer the properties of the TMDC

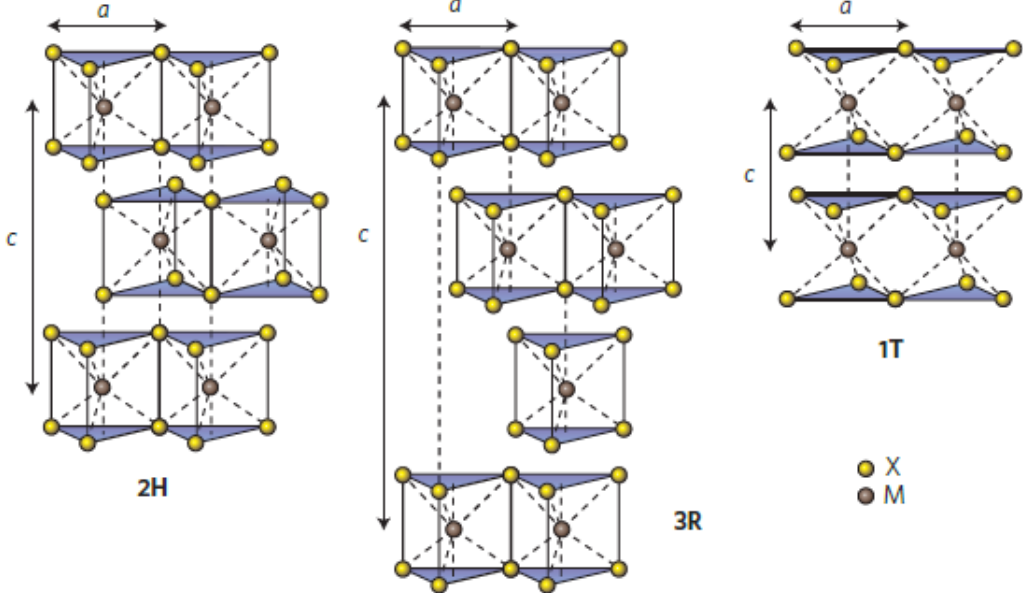


Figure 1: Schematics of the structural polytypes: 2H (hexagonal symmetry, two layers per repeat unit, trigonal prismatic coordination), 3R (rhombohedral symmetry, three layers per repeat unit, trigonal prismatic coordination) and 1T (tetragonal symmetry, one layer per repeat unit, octahedral coordination). The chalcogen atoms (X) are yellow and the metal atoms (M) are grey. The lattice constants  $a$  are in the range 3.1 to 3.7 Å for different materials. Adopted from [52]

undergo a significant change. In most TMDCs the bandgap changes from indirect to a larger direct one.

## 1.2 Electronic properties

One of the most interesting features that the layered TMDC materials exhibit is the shift in the bandstructure with the changing number of layers. Several studies have shown in simulations and experimentally that TMDCs have very similar electronic band structure as seen in example of  $WS_2$  in Figure 2. In bulk  $WS_2$  the maximum of the valence band (VBM) at  $\Gamma$  point and the minimum of the conduction band (CBM) at  $\Lambda$  form an indirect bandgap. As the number of the layers decreases the CBM at  $\Lambda$  point as well as VBM at  $K$  point increases causing the band gap to widen. At 2 layers the  $K$  point becomes the actual CBM and a new indirect bandgap forms between  $\Gamma$  point and  $K$  point. Finally in a  $WS_2$  monolayer the VBM at  $K$  point as well as entire conduction band increases to form a new greater direct band gap at  $K$  point. This means that  $WS_2$  bandgap changes from 1.3 eV indirect bandgap in bulk to 2.1 eV direct bandgap in monolayer.

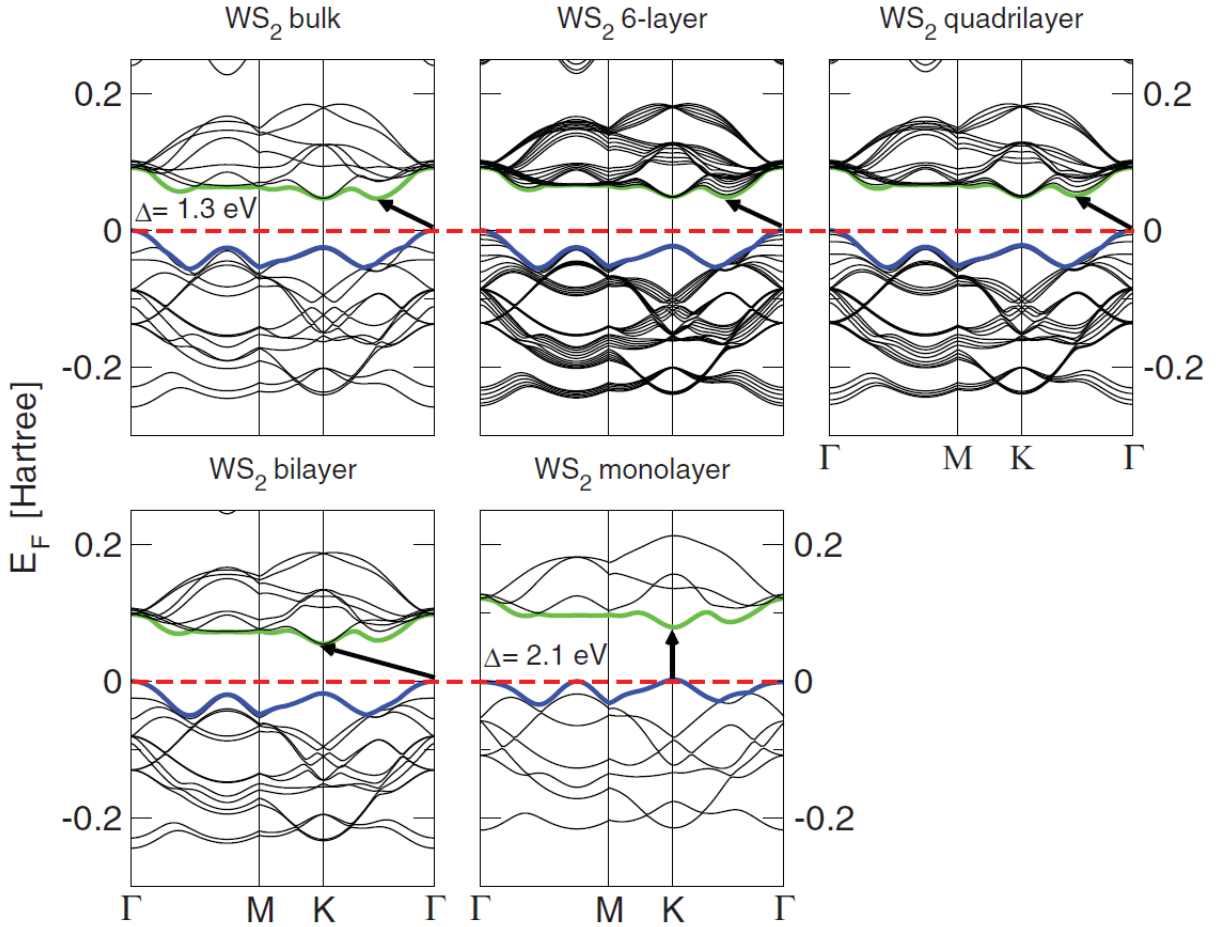


Figure 2: Band structures of bulk  $WS_2$ , its monolayer, as well as, polylayers calculated from the density functional theory (DFT) simulation. The horizontal dashed lines indicate the Fermi level. The arrows indicate the fundamental band gap (direct or indirect) for a given system. The top of valence band (blue) and bottom of conduction band (green) are highlighted. Adopted from Ref. [29]

Like  $WS_2$  other Mo and W based TMDC undergo similar transitions as seen in Table 1. In all cases the smaller indirect bandgap changes to greater direct bandgap with monolayer bandgap ranging from 1.1 eV to about 2.1 eV. Moreover the VBM at K points exhibits the orbit-spin band splitting at the K point of about 400 meV. This direct bandgap leads to presence of A and B excitons generated by transition between CBM and two VBMs at the K point. The conduction band as well as the valence band are dominated by the d-electron orbitals of the transition metal atoms and at the VBM and CBM they hybridize with the p-electron orbitals of the chalcogenide atoms. Because the hybridization happens mostly at the  $\Gamma$  point and the chalcogenide atoms are at the surface of the TMDC layer it leads to strong interactions between the layers. This leads to significant change in the

band structure at the  $\Gamma$  and rise of the indirect bandgap as a result of increased number of layers. On the other hand at the  $K$  point the d-orbitals of the transition metals remain mostly unaffected due to them being positioned in the middle of the layer [29] [49]

Table 1: Mo and W based TMDC bandgaps comparison

M\X	$-S_2$	$-Se_2$	$-Te_2$
Mo	Semiconducting	Semiconducting	Semiconducting
	1L: 1.8 eV	1L: 1.5 eV	1L: 1.1 eV
	Bulk: 1.2 eV	Bulk: 1.1 eV	Bulk: 1.0 eV
W	Semiconducting	Semiconducting	Semiconducting
	1L: 2.1 eV	1L: 1.7 eV	1L: 1.1 eV
	Bulk: 1.4 eV	Bulk: 1.2 eV	

### 1.3 Optical properties

TMDCs exhibit a wide array of opto-electronic effects due to their strong light-matter effects. These effects are mostly caused by the abundant presence of excitons, bi-excitons, trions or bound excitons. As a result the change in layer thickness from bulk to monolayer alters the photoluminescence, photoconductivity and absorption in the visible to infrared range.

The primary and most common quasi-particle that forms in such system is an exciton, which is a pair of a negatively charged electron and a positively charged hole bound together by Coulomb forces to form a structure similar to that of hydrogen atom. Such pair is electrically neutral and is of size exceeding size of single cell which makes it a Wannier–Mott exciton. The recombination of these excitons results in a photon emission which can be easily observed during photoluminescence characterisation. On top of excitons other quasi-particles such as trions, bi-excitons or bound excitons can be found. A trion is a group of 2 electrons and a hole or 2 holes and an electron, or otherwise described as a charged exciton. The exact nature of the trion depends usually on the type of intrinsic doping of the TMDC. A bi-exciton is a pair of excitons which is usually only observed in quantum dot systems but can be also seen in excitonically dense systems such as TMDCs. A bound exciton is similar to the free exciton but is trapped by a defect. In a typical photoluminescence spectrum several peaks can be observed depending on specific type of TMDC characterised. In  $WS_2$  monolayer for instance as seen in Figure. 3 the

strongest peak (often labelled as an A peak) at about 1.97 eV is caused by the direct transition of single-photon generated exciton. Slightly redshifted by about 30 meV from the A peak a generally weaker peak caused by the trion recombination can be found. At higher energies another peak can be observed due to the presence of bi-excitons. At around the 1.3 eV a much weaker peak (I) can be seen caused by the indirect transition. Additionally a B peak can be observed blueshifted from the A peak which is caused by valley splitting as discussed in chapter 1.2. As seen in Figure 3 as the number of layers increases the main A peak becomes dramatically weaker due to lack of direct transition and redshifted following the pattern discussed in chapter 1.2. At the same time the I peak becomes relatively stronger and eventually dominates the bulk material.

Figure 3: Typical PL spectra of  $WS_2$

Similarly the photoconductivity of the TMDCs is strongly reliant on the number of layers and incident photon energy. The  $MoS_2$  for instance shows 3 times stronger photoconductivity in monolayer around 1.8 eV, where the direct transition is located, than in 2L  $MoS_2$  around 1.6 eV. Additionally the photoconductivity appears to increase in steps with relation to the photon energy following the direct and indirect transitions. [52].

The sunlight absorption in TMDCs has been shown to be significantly more intense than in commonly used solar cell materials, at about 5-10% which is an order of magnitude greater compared to similar thickness of Si or GaAs. It is also stronger compared to 2-3% of sunlight absorption of graphene. As a result a excitonic solar cell based on  $MoS_2/WS_2$  bilayer shows about 1% power efficiency, about 3 times greater than that of typical ultrathin solar cells [3].

During standard single photon excitation photoluminescence studies the excitons generated can be called "bright" since they appear in PL spectrum. The reason we can observe them easily is because the spin between an electron and a hole is conserved, and thus allowing for photon emission. However another combination is possible, called dark exciton, where both electron and the hole have the same spin. Because of that they cannot recombine by emitting a photon and therefore remain absent from the PL spectrum. Even though they exist much longer than their bright counterparts their presence is of course also more difficult to observe. One way to observe them is to use two photon excitation. Due to two photon selection rule the single photon excitation can be excluded and the dark excitonic states can be observed. In  $WS_2$  the dark excitons result in two peaks at

2.28 eV and 2.48 eV. [Probing excitonic dark states in single-layer tungsten disulphide]

Defect engineering allows to tune the number of charge carriers. In MoS<sub>2</sub> or WS<sub>2</sub> the sulfur vacancies lead to increased number of electrons in the material. Because of that by increasing the number of defects in those materials the level of n-doping can be changed. An easy way to observe the presence of those defects and subsequent quenching of them is to expose the material to varying amounts of oxygen, nitrogen or water. Due to greater electronegativity (???) those species attract the electrons and therefore the electron population in the material decreases. This in turn leads to smaller trion population since trions require an extra electron to form. This then can be observed in PL as a more narrow direct peak, with especially smaller redshifted shoulder. The effect can also be of course reversed by decreasing the amount of oxygen, nitrogen or water in the environment since those exist in already in ambient conditions [Optical control of charged exciton states in tungsten disulfide].

In order to introduce and control the amount of vacancies in the TMDC different method have to be explored. One of the ways of achieving that in already grown material is the use of oxygen plasma. It has been shown that the number of defects can be controlled by limiting the plasma exposure. During the process the oxygen also chemically bonds to the MoS<sub>2</sub> at the defect sites and therefore partially negates the effect of defects on the optical properties. The PL can also be seen to increase in intensity with increasing number of defects with oxygen adsorbed due to the increased yield of bound excitons localised at these defects. [Strong Photoluminescence Enhancement of MoS<sub>2</sub> through Defect Engineering and Oxygen Bonding]

Similar effect has been shown using the 2,3,5,6-tetrafluoro-7,7,8,8-tetracyanoquinodimethane ( $F_4TCNQ$ ), 7,7,8,8-tetracyanoquinodimethane ( $TCNQ$ ) and (nicotinamide adenine dinucleotide)  $NADH$  for chemical doping. Both  $F_4TCNQ$  and  $TCNQ$  are p-type dopants while  $NADH$  is a n-type dopant. By exposing the surface of MoS<sub>2</sub> to these compounds the change in PL intensity and FWHM have been observed. Similar to doping with  $O_2$ ,  $N_2$  or  $H_2O$ , all of which are p-type dopants, the intensity of PL has increased in presence of  $F_4TCNQ$  and  $TCNQ$ . The effect has been similarly ascribed to lowering the number of defects and therefore the lowering the trion population and subsequently increasing the exciton population increasing the yield. The opposite observation has been made with use of  $NADH$  with PL intensity decreasing. Similarly the increase in trion population with lower PL yield is ascribed to the lower PL intensity. [Tunable Photoluminescence of Monolayer MoS<sub>2</sub> via Chemical Doping].

It has also been shown that alloying can be used to fine tune the PL by varying the concentration of alloying material. In monolayer  $Mo_{1-x}W_xS_2$  the PL peak position initially decreases from 1.575 eV (PL peak position of pure MoS<sub>2</sub>) to 1.56 eV at x=0.21 and then increase up to 1.65 eV (PL peak position of WSe<sub>2</sub>) at x = 1. This effect could be attributed to the linearity of VB and non-linearity of CB with regards to change in W composition. The PL position can therefore be engineered on a monotonic range from 1.56 eV to 1.65 eV. In bilayer  $Mo_{1-x}W_xS_2$  alloy the position of both direct and indirect transition PL peaks increases monotonically from about 1.49 eV and 1.53 eV for pure MoSe<sub>2</sub> to 1.56 eV and 1.62 eV for pure WSe<sub>2</sub> as the W amount is increased. This opens another relatively easy way of engineering PL position [Two-Dimensional Molybdenum Tungsten Diselenide Alloys: Photoluminescence, Raman Scattering, and Electrical Transport].

Another effect that has been demonstrated that allows for certain degree of control of PL in TMDCs is relation between the helicity of incident light and valley population valley population. It has been shown that by exciting the monolayer  $MoS_2$  with right-polarised light the resulting excitons will fill primarily the VB at K point. Similarly by exciting the  $MoS_2$  with left-polarised light the excitons will fill the VB at K' point. After recombination the resulting photons will exhibit the same circular polarity as the photons that excited the electrons in the first place. [Tightly bound trions in monolayer MoS<sub>2</sub>] [Control of valley polarization in monolayer MoS<sub>2</sub> by optical helicity]

The temperature effect on TMDCs has also been investigated. In  $WSe_2$  monolayer it has been shown that as the temperature of the sample increases from room temperature to about 400K the position of the direct transition PL peak redshifts from about 1.65 eV to about 1.58 eV. When the temperature is decreased from room temperature to about 5K the same peak blueshifts to about 1.7 eV. Between 100K and 50K as well 20K and 5K the position of the PL peak does not change. Additionally around 120K another peak appears and as the temperature is lowered it also blueshifts although less than the RT peak. The peak only present at RT is attributed to free excitons whereas the peak appearing at 120K is ascribed to bound excitons. As bound exciton peak appears its intensity increases with lower temperature while the intensity of the free exiton peak decreases. This indicates that the population of free excitons decreases while the population of the bound excitons increases with decreasing temperature [50]

There has been many reports on the spatial distribution of PL in the TMDCs. One of the observed patterns in WS<sub>2</sub> and MoS<sub>2</sub> has been that of much stronger PL intensity at the edges of the flakes. That effect has been primarily observed in small flakes of about

$5 \mu m$  [16].

## 1.4 Phonon dispersion

The vibrational and phononic characteristics of TMDCs have been investigated at length by both theoretical simulations as well as experimental studies. The  $2H - MX_2$  crystal structure of the TMDCs belongs to  $D_{6h}^4$  point group and there are 18 lattice dynamical modes at the  $\Gamma$  point. Phonons belonging to these modes can be represented as Eq. 1 [53]:

$$\Gamma = A_{1g} + 2A_{2u} + B_{1u} + 2B_{2g} + E_{1g} + 2E_{1u} + E_{2u} + 2E_{2g} \quad (1)$$

In TMDCs 4 active Raman modes can be observed  $E_{1g}$ ,  $E_{2g}^1$ ,  $E_{2g}^2$ ,  $A_{1g}$ . These can be seen in Figure 4. The  $E_{2g}^2$  is a shear mode that involves 2 layers vibrating against each other. The  $E_{1g}$  is an in-plane vibration of chalcogen atoms but is forbidden in the back-scattering configuration. For monolayers therefore it leaves primarily the  $E_{2g}^1$  which is an in-plane mode involving vibration of both metal and chalcogen atoms as well as  $A_{1g}$  which is an out-of-plane mode involving only chalcogen atoms.

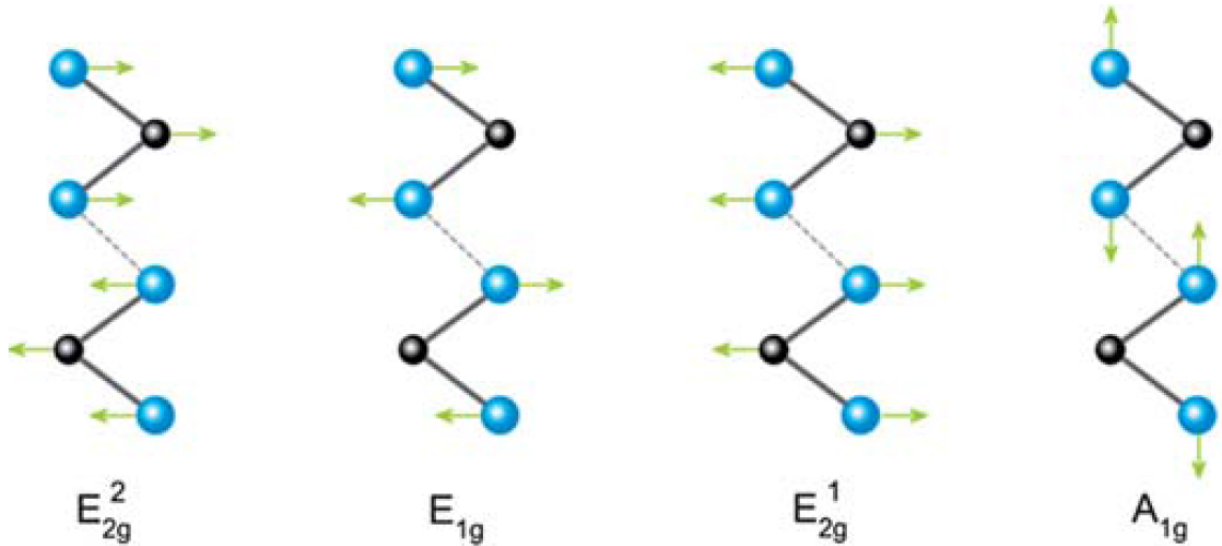


Figure 4: 4 active Raman modes in TMDCs. Metal atoms and chalcogen atoms are black and blue respectively. Adopted from [53]

These two peaks tend to dominate the spectrum of any TMDCs, whether monolayer or few-layer or bulk. The shear mode  $E_{2g}^2$  appears at low Raman shift frequencies and is therefore difficult to observe but can be used to differentiate monolayer from few-layer

material. Since  $E_{2g}^1$  is an in-plane mode it tends to be unaffected by the number of layers due to weak van der Waals forces between the layers but can be seen to be slightly redshifted as the number of layers increases. As seen in Figure 5 the  $E_{2g}^1$  peak at about  $352\text{ cm}^{-1}$  is overlapping with another stronger peak, a 2LA(M) peak at  $350\text{ cm}^{-1}$  which is a longitudinal acoustic mode caused by in-plane collective oscillations of W and S atoms. The second strongest peak at around  $416\text{ cm}^{-1}$  is an  $A_{1g}$  peak, caused by out of plane vibrations. Because of that it is much more sensitive to the number of layers and is seen to become blueshifted as the number of layers increases. This has been attributed to the restorative forces as well as increase in dielectric screening of the Coulomb forces. Combining both of these shifts in frequency with the changing number of layers the difference between these two peak position can be used to identify the number of layers in TMDCs as seen in Figure 6

Figure 5: Typical Raman spectrum of  $WS_2$

Figure 6: Identification of number of layers by the difference in position of  $A_{1g}$  and  $E_{2g}^1$  peaks.

## 2 Role of precursors in growth of monolayer $WS_2$

In this chapter the CVD growth of  $WS_2$  using different precursors is investigated. The as grown samples were characterised by Raman and PL spectroscopy as well as XPS, XRD, AFM and electrical measurements. As a result it was concluded that using  $H_2WO_4 + NaCl$  at 850 °C gives best results. Such grown samples exhibit biggest flakes up to 200  $\mu m$  in size as well as show the strongest and most narrow PL peak with 36 meV FWHM. The samples grown using  $H_2WO_4 + NaCl$  at 950 °C show also best transistor electron mobility in monolayer CVD grown  $WS_2$  while that grown using  $WO_3 + NaCl$  at 950 °C shows best transistor electron mobility in bilayer CVD grown  $WS_2$ .

### 2.1 Introduction

Monolayers of transition metal sulphides and selenides exhibit range of interesting properties such as strong light absorption in the IR and visible range [40][3][64], valley polarisation [39] [20], spin-orbit interactions [58][65], tightly bound excitons [38] or second-harmonic generation [34]. Some of these effects can be attributed to the lack of free dangling bonds and configuration of d-orbitals [54], [33].

Among these materials one of the most promising is the  $WS_2$ . Its visible range bandgap of 2eV as well as an easy and safe manufacturing route via CVD makes it one of the more interesting and studied TMDCs. The typical characterisation by photoluminescence spectroscopy allows to probe the varying synthesis conditions, the grain boundaries or defect population [16] [44] [32] [47]. The PL efficiency in as-grown monolayer  $WS_2$  produced via CVD growth shows ~2-6% efficiency [44][60] [35]. This efficiency is caused mostly by defect-mediated non-radiative recombination centres [2]. LEDs have been successfully produced [26] showing external quantum efficiency up to 10% [62][55].  $WS_2$  is typically a n-type semiconductor due to the presence of sulphur vacancies [16][48][23]. In order to utilise this material in any potential future applications a reliable and scalable manufacturing method must be developed to ensure a high quality crystal on the wafer scale area. The main method for  $WS_2$  synthesis that satisfies these conditions is Chemical Vapour Deposition (CVD) [17]. The growth of tungsten based TMDCs have been less successful than the equivalent molybdenum based TMDCs and has produced mostly isolated flakes of up to 40  $\mu m$  [16] [63] [47] [10][59][11][31]. Even larger films of monolayer  $WS_2$  have been shown, however they also exhibit low carrier mobility [27][12]. In the typical CVD synthesis process the sulphur and tungsten oxide are evaporated simultaneously in

a tubular furnace with a constant flow of carrier gas like argon at temperatures of at least 900 °C [16][63][47][10][59][11][31]. Such growth is predicated by topotactic transformation leading to low density distribution of domains on an amorphous [16][63][10][11][31] or crystalline substrate [47][59][42] possibly due to low evaporation rates of  $WO_3$ . Since  $WO_3$  requires high temperatures of 950-1000 °C to evaporate while the  $S$  becomes volatile at 90 °C the thermodynamics of the process are difficult to control. The low growth dictated by fast evaporation of  $S$  leads to limited domain growth and lack of continuous layer. One of the proposed solutions have been to spread the  $WO_3$  on the target substrate [44][32][12][6][61][15][14]. This has however led to low reproducibility, poor control of thickness and stoichiometry and unreacted material left on the substrate. Another approach has been to use more volatile  $W$  precursors such as  $WCl_6$ [4] or  $W(CO)_6$ [27][9] together with organic compounds as  $S$  precursors. Such method while producing a large area domains at lower temperature has led to lower crystal quality and purity.

Here we propose a different method of CVD synthesis that allows for much larger flake growth of up to 800  $\mu m$  at temperature of 750 degreeC. Such grown material exhibits high electron mobility in one and two layers of  $WS_2$ , higher than other values reported in literature. The photoluminescence peak is also very narrow at 36 meV FWHM at room temperature.

## 2.2 Results

For the purpose of comparing the CVD synthesis method conditions the several sets of precursors were used:  $WO_3$ ,  $WO_3 + NaCl$  and  $H_2WO_4 + NaCl$ . The standard growth procedure involves two separate crucibles placed at distance from each other in a quartz tube. Each of these crucibles is independently heated to ensure that the S and the W precursors evaporation rate is maximised at the same time. The vapours then are deposited on  $SiO_2/Si$  (285 nm) substrate which is placed close to the W precursor crucible. The entire process is performed under low vacuum and a supply of Ar gas. The furnace setup can be seen in Figure 7.

By following this method a reproducible deposition of large area flakes can be shown. As seen in Figure 8 the size of the flakes increases from left to right as the precursors used ( $WO_3$ ,  $WO_3 - NaCl$  and  $H_2WO_4 - NaCl$ ) change as well as demonstrating the lower temperature required to achieve these growths. All of these growths result in formation of triangular flakes with sharp edges and uniformity of colour throughout which suggest

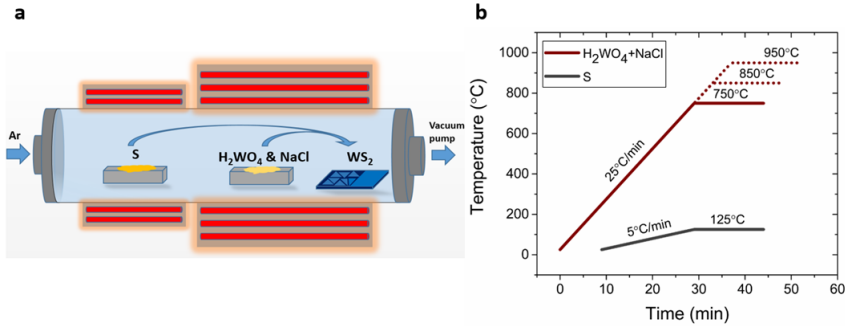


Figure 7: Illustration of: (a) CVD tubular furnace set-up; (b) temperature profile of the sulphur and the W-precursors heaters respectively. The sulphur reaches 125 °C when the metal precursors are at the maximum temperature. The SiO<sub>2</sub>/Si wafers used as substrate for WS<sub>2</sub> growth are placed 1-8 cm downstream the W-precursors crucible and they are subjected to the same temperature.

a high quality, pristine material across the flake. The growth using only  $WO_3$  results in formation of small flakes of 10  $\mu m$  at 950 °C while no growth occurs at lower temperatures (Figure 8. This can be explained by the high sublimation temperature of  $WO_3$ .

The growth can also be observed using  $WO_3 + NaCl$  at 950 °C and 850 °C with the former showing flakes of size of about 60  $\mu m$  while the latter showing smaller flakes of about 30  $\mu m$  in size. To explain this difference in size a Robinson & Robin model can be used which states that at higher temperatures the diffusivity of the adsorbed precursors is favourable to the expansion of the existing domains. On the other hand the desorption of the adsorbed species is high leading which limits the supersaturation and formation of new domains. If the temperature is lowered even further to 750 °C then no growth is observed at all, most likely due to slow evaporation of  $WO_3$  precursor.

With the change of precursors from  $WO_3$  to  $H_2WO_4$  a signifacnt change in size of flakes is observed at 850 °C and higher temperatures with lengths exceeding 200  $\mu m$ . Additionally the growth have been shown to occur at 750 °C with flakes of the size of 50-200  $\mu m$ . Moreover continuous monolayer areas of up to 0.8 mm in size has been shown (Figure ??). By increasing the growth pressure (1.6 mbar to 13 mbar) at 950 °C bilayer  $WS_2$  flakes can be preferentially formed (Figure ??).

Original paper starts here. To be replaced or rewritten

By replacing  $WO_3$  with  $H_2WO_4$  the lateral size of the  $WS_2$  monolayered domains significantly increases (Figure 1g,h,i). The triangular crystals have edge lengths exceeding 200  $\mu m$  at temperatures higher than 850 °C and between 50-200  $\mu m$  at 750 °C (Fig-

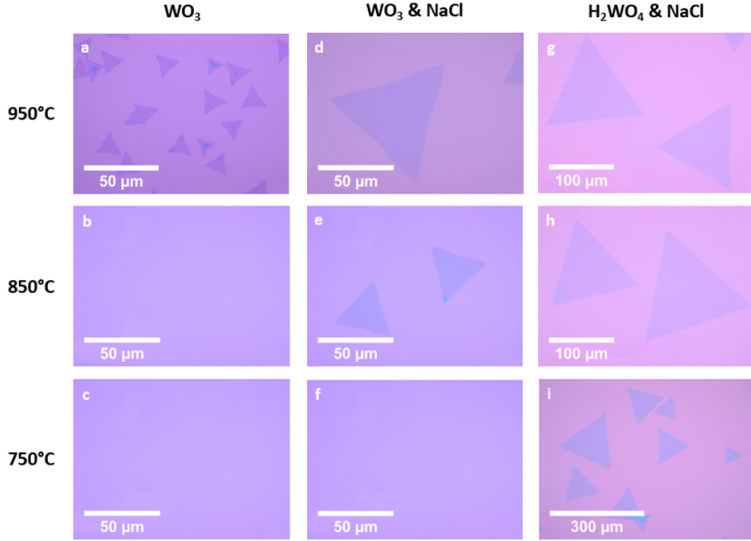


Figure 8: Optical micrographs of  $WS_2$  triangles grown on  $SiO_2/Si$  substrates at different temperatures and using different precursors: (a)  $WO_3$  at 950 °C; (b)  $WO_3$  at 850 °C; (c)  $WO_3$  at 750 °C; (d)  $WO_3 + NaCl$  at 950 °C; (e)  $WO_3 + NaCl$  at 850 °C; (f)  $WO_3 + NaCl$  at 750 °C, the OM appears as a bare  $SiO_2$  substrate; (g)  $H_2WO_4 + NaCl$  at 950 °C; (h)  $H_2WO_4 + NaCl$  at 850 °C; (i)  $H_2WO_4 + NaCl$  at 750 °C.

ure 1g,h,i). Continuous polycrystalline monolayer coverage has been obtained over areas of  $\sim 0.8$  mm extension (Figure S2). Increasing the growth pressure (from 1.6 mbar to 13 mbar) at 950 °C bilayered  $WS_2$  flakes are preferentially formed (Figure S3). To understand the facilitated synthesis of  $WS_2$  using  $H_2WO_4$  and  $NaCl$ , we conducted X-ray diffraction (XRD) analysis of the reaction products between  $H_2WO_4 + NaCl$  and  $WO_3 + NaCl$  systems at different temperatures (500 °C, 650 °C and 750 °C) to understand the chemical differences (Figure S4). We found that the main products of the reactions between  $NaCl$  and  $H_2WO_4$  are:  $NaxWyOz$  and tungsten oxychloride ( $WClO_4$  and  $WO_2Cl_2$ ). The  $NaxWyOz$  possesses a high evaporation temperature as it remains in the crucible (Figure S5) after the synthesis of  $WS_2$  is completed. Further, using this compound as precursors for a new growth of  $WS_2$  at 950 °C did not lead to the formation of any  $WS_2$  flakes, confirming the high evaporation temperature. On the bases of previous studies on the synthesis of bulk crystals, the formation of tungsten oxychloride species ( $WO_2Cl_2$  and/or  $WOCl_4$ ) is likely to occur while the formation of metal halides is less favourable (e.g.  $WCl_6$ ) [ ][ ]. Tungsten oxychlorides are volatile already at 200 °C [ ] and they can be sulfidized in vapour phase and then be deposited onto the target substrate as atomic clusters.  $WOCl_4$  has been previously used [43] as precursor for the CVD synthesis of  $WS_2$  bulk films. De-

spite its strong tungsten oxygen double bonds, WOCl<sub>4</sub> proved to be an effective precursor with a clean decomposition pathway in the CVD process without formation of tungsten oxysulfide. We have verified that using this precursor is indeed possible to obtain WS<sub>2</sub> at temperatures as low as 550 °C (Figure S6a). The key role played by the oxyhalide species it becomes apparent if we try to grow WS<sub>2</sub> by using only hydrated tungsten oxide. As this decomposes to form WO<sub>3</sub>, only small WS<sub>2</sub> domains are observed with similar PL characteristics to the WO<sub>3</sub> precursors-growth (Figure S6b). Furthermore, to confirm the key role played by Cl, we replaced NaCl with KCl and we obtained comparable growth results (Figure S6c).

### End of paper

### Incorporate XRD

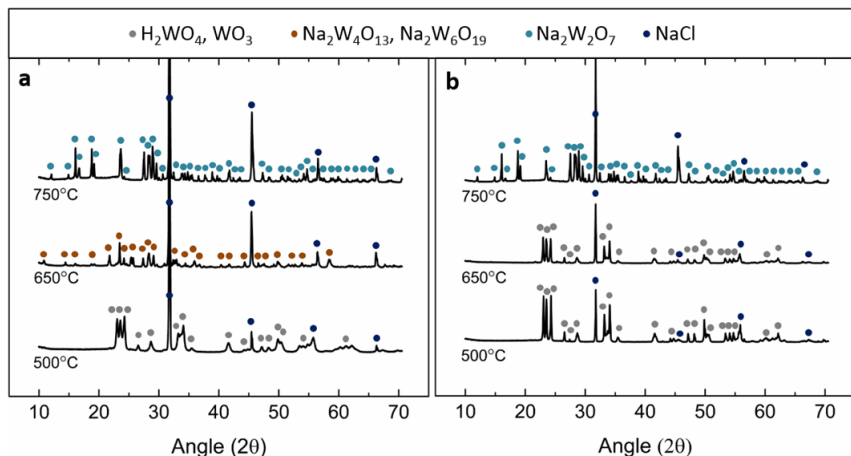


Figure 9: XRD pattern of the residual powder of W-precursors after thermal treatment at 500 °C, 650 °C and 750 °C respectivley, using (a) H<sub>2</sub>WO<sub>4</sub>+NaCl and (b) WO<sub>3</sub>+NaCl as precursor.

The flakes were investigated using HRTEM to confirm high crystallinity of the material (Figure 11. The lattice constant measured in this way has been found to be 0.3 nm, which is consistent with that of 2H-WS<sub>2</sub> (0.318 nm). The AFM characterisation allowed to confirm the presence of monolayer (Figure 11) and bilayer (Figure ?? flakes with the step of 0.8 nm [57][46].

The Raman spectroscopy characterisation of WS<sub>2</sub> flakes obtained under different growth conditions can be seen in Figure 11. All of these spectra exhibit the main 2 peaks at  $\sim(351\pm0.53)$   $cm^{-1}$  and  $\sim(417.6\pm1)$   $cm^{-1}$ . The latter peak corresponds to the  $A_{1g}$  vibrational mode while the former peak can be further resolved into two peaks, one related to 2LA vibrational mode and the second to  $E_{2g}^1$ . As seen in the Figure 14a and

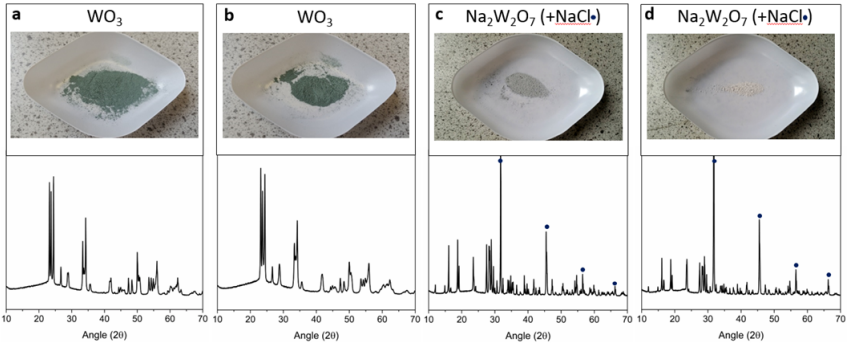


Figure 10: Residual powders of the W-precursors and their XRD patterns after thermal treatment at 750°C using (a)  $WO_3$ , (b)  $H_2WO_4$ , (c)  $WO_3+NaCl$ , and (d)  $H_2WO_4+NaCl$  as precursor. The blue dots in the XRD patterns indicate the presence of residual  $NaCl$ .

Figure 14c the distribution of intensity of both main peaks is uniform across the flakes. Similarly the difference between peak positions of  $A_{1g}$  and  $E_{2g}^1$  is also uniformly distributed as seen in Figure 15 and is equal to  $\sim(66.5\pm0.53)$   $cm^{-1}$  which is indicative of monolayer [56].

As seen in Figure 12 maps of PL intensity has been collected for samples grown using different growth condition. The sample grown using  $WO_3$  at 950 °C appears to be trisected into 3 symmetrical areas. The intensity is lowest along the the trisecting lines and highest in the centre of each of the sub-triangles. The PL peak position is inversely proportional to the intensity of the PL peak as seen in Figure 16a. The distribution of the PL peak positions seems to be bimodal with maxima at 1.96 eV and 1.94 eV. The FWHM is distributed mostly uniformly with few small areas of greater and few of smaller FWHM (Figure 16b with the average value of 65 meV. These peak position and FWHM values are comparable with those reported in literature [16][47][18][28]. The PL spectra taken from one of the three smaller parts of the flake are redshifted by about 0.02 eV and are wider than average. This can be explained by the presence of defects, in particular sulfur vacancies, which effectively cause the  $WS_2$  to be n-doped [21][45]. This in turn increases the trion population which introduces new peak, redshifted by about 30 meV, which results in overall shift and broadening of the PL peak [51][16]. Additionally such localised changes in PL peak intensity and position can be caused by local strain [37][21]. To investigate the potential effect of strain on the observed PL pattern a flake was cut using high power 532nm laser. As seen in Figure 17 the resulting pattern remains the same as before treatment. Therefore the observed pattern is most likely caused by the local variation in defect density [36].

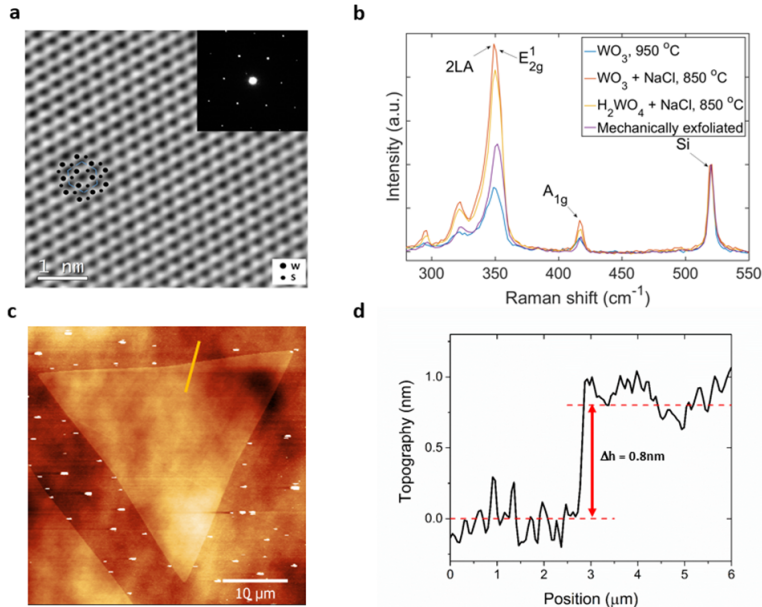


Figure 11: Structural and physical characterization of  $WS_2$  triangles: (a) HRTEM image of the  $WS_2$  lattice grown using  $H_2WO_4 + NaCl$ , the inset report a selected diffraction area which show a hexagonal pattern. (b) Raman spectra showing the characteristics active modes of  $WS_2$  grown under different conditions and compared with mechanically exfoliated flakes. (c) AFM image and (d) corresponding thickness profile of monolayer  $WS_2$ .

By introducing the  $NaCl$  and mixing it with  $WO_3$  precursor  $WS_2$  samples are grown that exhibit higher energy and narrower PL peaks. The spectra are asymmetric and can be therefore deconvoluted to obtain an exciton and trion component (Figure 13). The spatial distribution of the PL position and width is mostly uniform throughout the flake. However the distribution of PL peak positions and FWHM across different flakes grown at the same conditions is bimodal (Figure 13). The PL peak position is found to be ( $\sim 1.95 \pm 0.002$  eV and  $1.96 \pm 0.002$  eV) while the FWHM is ( $\sim 43 \pm 2.8$  meV and  $51 \pm 3$  meV) which is smaller than most reported works [16][47][18][28]. This can be explained by smaller trion component in the PL spectrum which in turn means that  $WS_2$  samples grown at these conditions contain less structural defects compared to the pure  $WO_3$  growth. A difference in growth mechanism (topotactic or molecular conversion) which results in different defect distribution can be attributed to the differences in samples.

By changing the  $WO_3$  precursor to the  $H_2WO_4$  precursor a further shift in PL peak position, as well as increase in PL intensity and narrowing of he PL peak is observed as seen in Figure 12, 13. The PL peak position distribution across the flake is narrow and

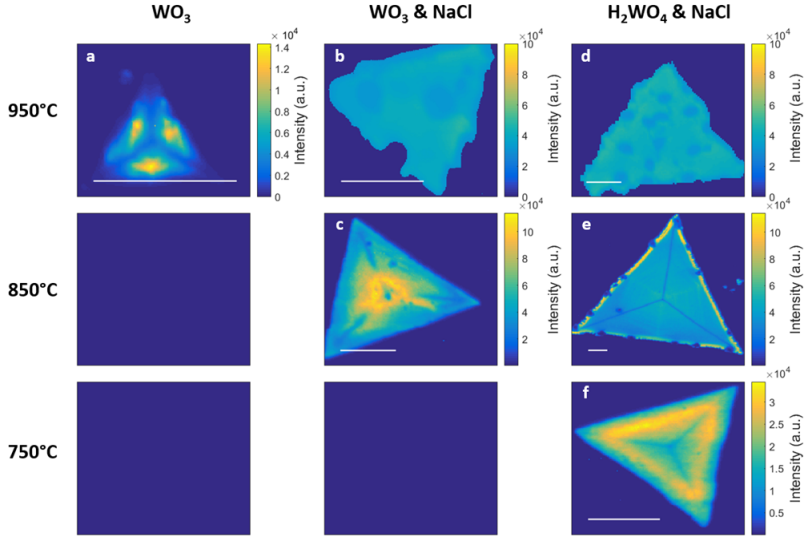


Figure 12: Spatial maps of PL intensity of  $WS_2$  grown in the conditions exemplified in Figure 1. The scale bar length is  $10\mu m$ .

is ( $\sim 1.980 \pm 0.005$  eV) which is higher than that of the  $WO_3$  and  $WO_3 + NaCl$  systems. The FWHM is found to be ( $\sim 36 \pm 3$  meV) which is also smaller than that of the  $WO_3$  and  $WO_3 + NaCl$  systems. The PL peak width is also smaller than that reported in literature for CVD grown [16][47][18][28] exfoliated  $WS_2$  [64][48]. At the same time it is comparable to the  $WS_2$  grown on van der Waals substrates [42] as well as mechanically exfoliated  $WS_2$  [26]. Additionally the peak position as well as FWHM variation is also smaller than that of other samples (5meV and 3meV respectively) (Figure 18d. The PL peak intensity map (Figure 12) shows that the spatial distribution of intensity is also much more homogeneous with faint weak pattern of three trisecting lines still visible.

### Incorporate PL maps and scatter plots

As seen in Figure 14 the Raman peaks are generally uniform in both intensity and position for most samples. The irregularities in the intensity and position of both the  $E_{2g}^1$  and  $A_{1g}$  in the sample grown at 950 °C with both  $WO_3 + NaCl$  and  $H_2WO_4 + NaCl$  are caused primarily by residue deposited on top of the flakes after the growth as seen in optical micrographs. Additionally as seen in Figure 14a the deviations from the mean value are located primarily at the edges of the sample. This suggests that the rest of flake is pristine and the deviations are associated with residue located at the edges. The coefficient of variation (CV) for the intensity and position for the samples grown at 950 °C with  $WO_3$  and at 850 °C with  $WO_3 + NaCl$  and  $H_2WO_4 + NaCl$  is on the order of up to  $10^{-4}$  which indicates a very high homogeneity across the samples. This further shows

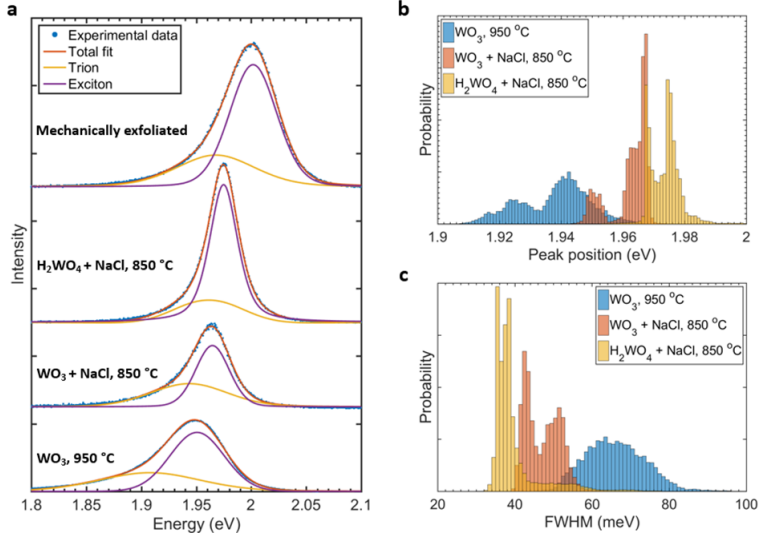


Figure 13: PL spectra characteristics of WS<sub>2</sub> grown using: WO<sub>3</sub> at 950 °C, WO<sub>3</sub>+NaCl at 850 °C, H<sub>2</sub>WO<sub>4</sub>+NaCl at 850 °C: (a) individual spectra (dotted line) and deconvolution in exciton and trion components; (b) distribution of PL peak position and (c) distribution of PL FWHM for several WS<sub>2</sub> grown using the three different precursor systems.

that the crystal quality of the flakes is quite uniform regardless of the growth method.

By looking at the difference in position between  $A_{1g}$  and  $E_{2g}^1$  peak positions as seen in Figure 15 it can be further concluded that the flakes are uniformly monolayer. The deviations from the mean are heavily localised and correlated with differences in PL as well as optical images and are most likely caused by precursors residue. Additionally no trisecting lines (as seen in Figure 12) can be seen in the maps of Raman spectra.

The maps of PL peak positions and widths can be seen in Figure 16. The PL positions map of the sample grown at 950 °C using  $WO_3$  shows some variability with spots of lower energy that loosely correlate with the PL intensity. There is still faintly visible pattern of three trisecting lines of higher energy as seen in Figure 12. This indicates the areas with higher intensity correlate with lower peak position, especially along the trisecting lines. The other maps, especially the ones grown at 850 °C and 750 °C with  $WO_3 + NaCl$  and  $H_2WO_4 + NaCl$ , are more uniform in terms of PL peak position and PL peak width. The deviations are again highly localised and correlated with the deviations in Raman and PL intensity. These deviations are generally of lower PL peak position as well as greater PL peak width which generally indicates lower crystal quality.

One possible explanation of the pattern of trisecting lines as seen in e.g. Figure 12 is the thermal strain caused by difference in thermal expansion coefficient between  $WS_2$  and

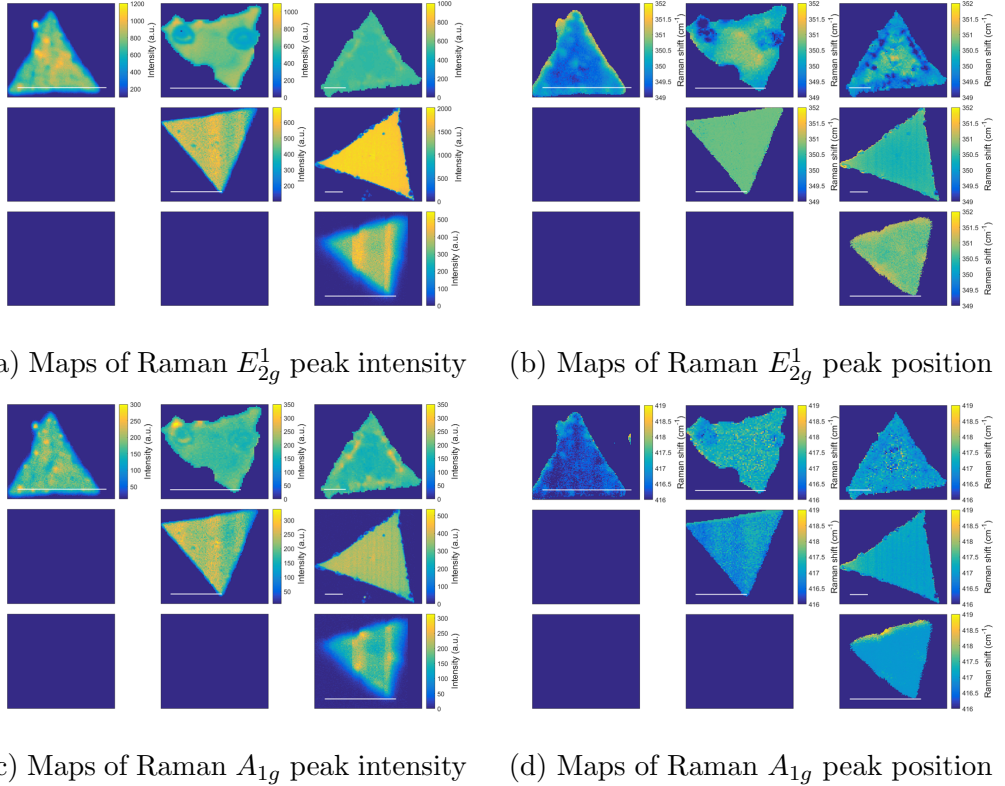


Figure 14: Maps of Raman peaks intensities and positions

the  $SiO_2$  substrate. Since it is known that the strain in TMDCs including  $WS_2$  can cause the change in Raman and PL spectrum [37][21] then removing a piece of the material should cause the strain to adapt to new bounding conditions. In order to investigate the trisecting pattern a flake with such pattern has been cut using 532 nm high intensity laser (50 mW). As seen in Figure 17 both the PL intensity maps and Raman  $E_{2g}^1$  maps show a clear separation. The resulting PL and Raman intensity maps however do not show any significant change in the pattern. The trisecting lines as well as local maxima can still be seen in PL intensity map. The Raman shows few spots of increased intensity on the halves of the flake as well as a very weak increased intensity area along the cut. Since there is no observed increased intensity along any edges before cutting the flake it does not appear that the increased intensity along the cut is a result of strain being resolved into new bounding conditions. It appears therefore that cutting the material did not alter the pattern nor alter the rest of the PL or Raman spectra maps.

The spectral maps from different flakes grown with the same conditions were then collected and plotted as graphs of intensity or width versus position. As seen in Figure 18d the PL intensity seems to be largely independent of the PL position. If PL is present at given position then intensity is mostly uniformly distributed in terms of intensity. The

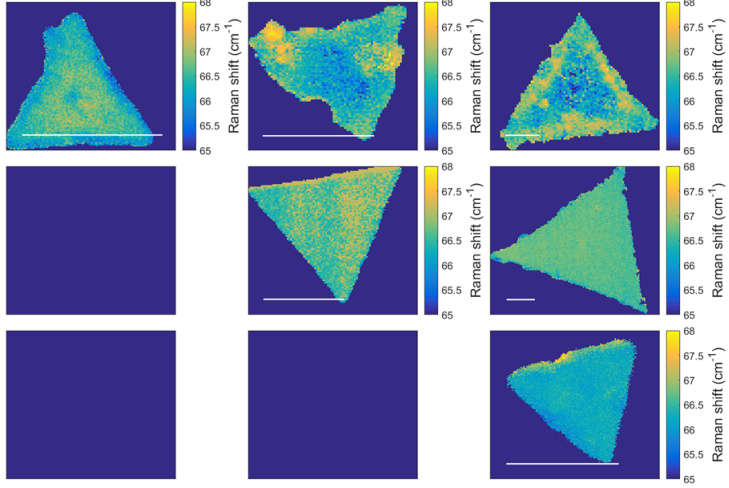
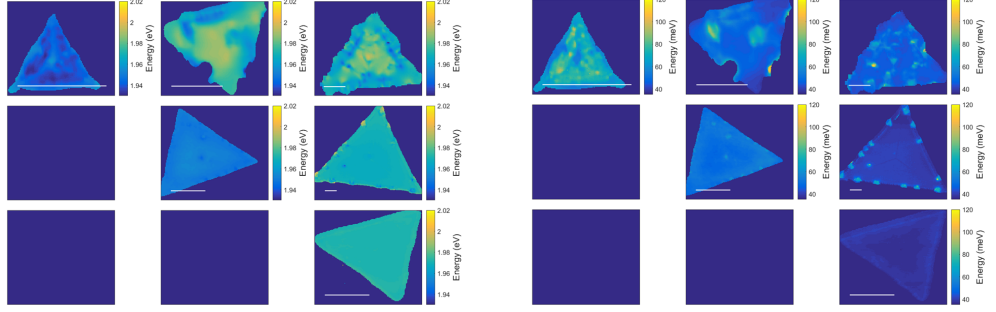


Figure 15: Raman spectroscopy:  $2LA - A_{1g}$  energy differences. Scale bar is  $10 \mu\text{m}$



(a) Maps of PL peak position

(b) Maps of PL peak width

Figure 16: Maps of PL peak positions and width

PL width seems to be inversely related with regards to PL position. In samples grown at  $850^\circ\text{C}$  with  $WO_3 + NaCl$  the relation seems to be the strongest. Across all the samples the values vary between around 60-80 meV at low PL energies (1.92 eV) to 40-60 meV at high PL energies (1.98 eV). This seems to be related to overall quality of the crystals, i.e. the presence of defects, stoichiometry, crystallinity, doping, adatoms. The more uniform the sample the less mechanisms for peak broadening as well as fewer added energy levels facilitating different electron recombination paths.

The chemical composition of the flakes grown using  $H_2WO_4 + NaCl$  has been investigated using XPS. The W 4f $5/2$  and W 4f $7/2$  core levels show peak positions that of the  $W^{4+}$  in  $WS_2$  [5][41] (32.7 eV 34.8 eV respectively) with FWHM of 1 eV (Figure 19, the smallest possible using Mg K $\alpha$  x-ray source. It means therefore that the  $WS_2$  is of perfect stoichiometric ratio of W and S. Additionally by integrating the intensity of the

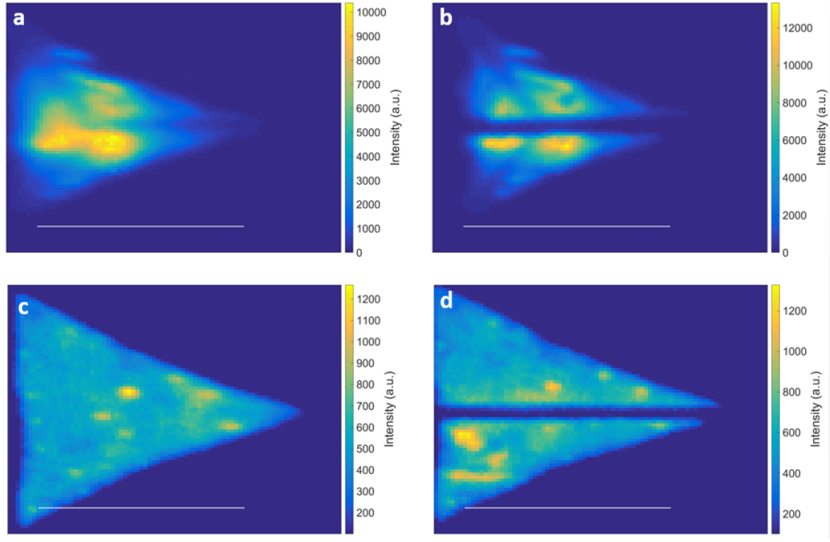
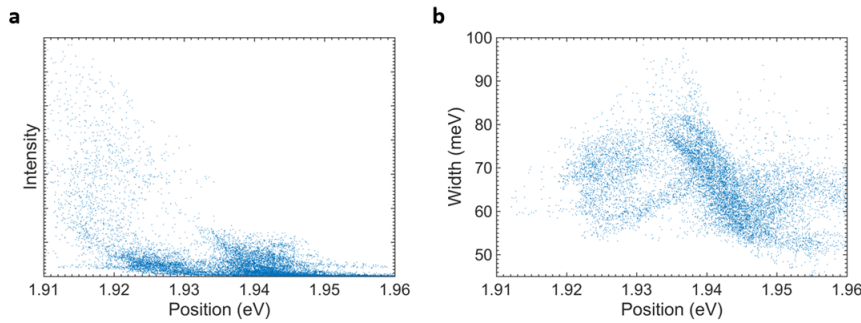


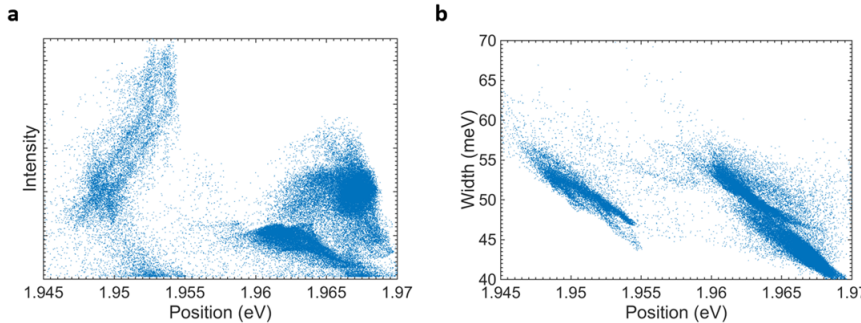
Figure 17: PL intensity (a) before and (b) after the cutting.  $2LA + E_{2g}^1$  Raman intensity (c) before and (d) after the cutting. Scale bar is  $10 \mu m$

$W\ 4f$  and  $S\ 2p$  core level peaks the same result is achieved. Furthermore the  $S\ 2p1/2$  and  $2p3/2$  core levels are also present at the expected position for  $WS_2$  (162.3 eV and 163.4 eV respectively, Figure 19) and small FWHM of 1 eV [41]. Small peaks indicative of  $W^{6+}$  ( $W\ 4f5/2$  and  $W\ 4f7/2$  at 35.9 eV and 38.1 eV respectively, Figure 19) can be attributed to presence of  $WO_3$  and which partially overlaps with  $W\ 5p$  core level (38.5 eV). These peaks however disappear after the flakes are transferred to another  $Si/SiO_2$  substrate, suggesting that they can be caused by residue  $WO_3$  given that the XPS spot size is relatively big ( $\sim 1$  mm). The FWHM of the  $W\ 4f$  core levels was unchanged after the transfer, indicating that the crystallinity and the quality of the flakes was preserved with no extra defects introduced.

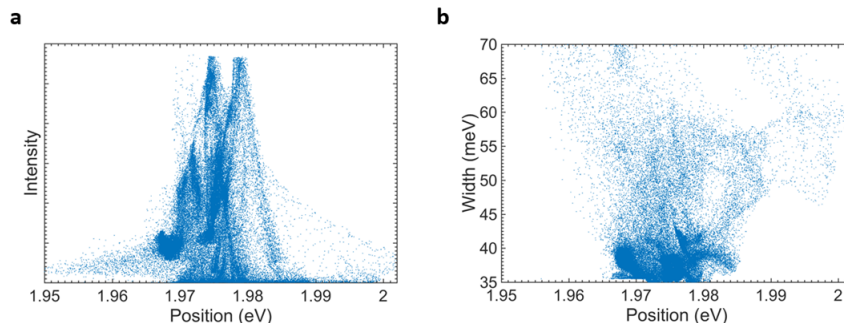
The  $WS_2$  samples grown using  $WO_3 + NaCl$  have been characterised by XPS as well and the stoichiometric ratio of 2:1 for S:W has been found. However the  $W^{6+}$  component, caused most likely by presence of  $WO_3$  ( $W\ 4f5/2$  and  $W\ 4f7/2$  at 35.9 eV and 38.1 eV respectively) is more pronounced indicating incomplete sulfurisation. Similarly to the sample grown with  $H_2WO_4 + NaCl$  this component disappears entirely upon transferring the sample onto new  $Si/SiO_2$  indicating it is present around the flakes, distributed across the substrate. The  $W^{4+}\ 4f$  core levels peak width is  $\sim 1.2$  eV which indicates higher defect concentration compared to that of the sample grown using  $H_2WO_4 + NaCl$ . This FWHM however increases after the transfer, which is most likely caused by the increase in the concentration of the defects caused by the mechanical stress during the transfer.



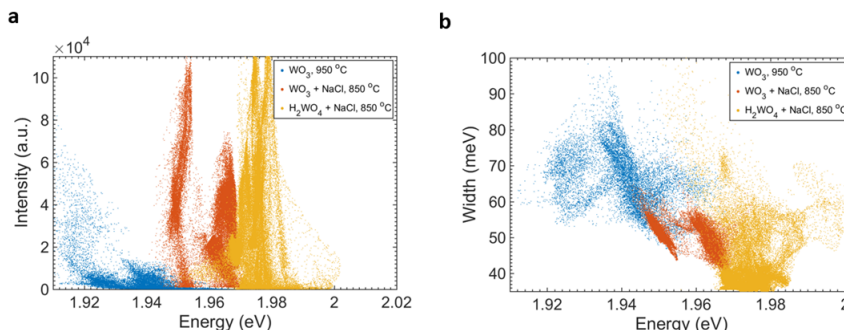
(a) (a) PL Intensity vs position, (b) PL FWHM vs position of  $WS_2$  grown using  $WO_3$  at 950 °C



(b) PL Intensity vs position, (b) PL FWHM vs position of  $WS_2$  grown using  $WO_3 + NaCl$  at 850 °C



(c) (a) PL Intensity vs position, (b) PL FWHM vs position of  $WS_2$  grown using  $H_2WO_4 + NaCl$  at 850 °C



(d) (a) PL Intensity vs position, (b) PL FWHM vs position of  $WS_2$  grown using  $WO_3$ ,  $WO_3 + NaCl$ ,  $H_2WO_4 + NaCl$

In conclusion the  $H_2WO_4$  is shown to be a better precursor compared to  $WO_3$ .

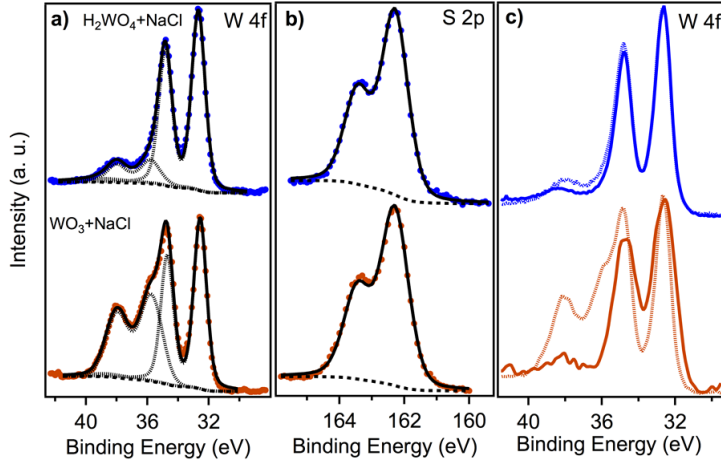


Figure 19: XPS spectra of the W 4f and S 2p core level peak regions. (a) Comparison of W 4f<sub>5/2</sub>, W 4f<sub>7/2</sub> and W 5p core levels of WS<sub>2</sub> grown using H<sub>2</sub>WO<sub>4</sub>+NaCl at 950 °C (blue spectrum) with WS<sub>2</sub> grown using WO<sub>3</sub>+NaCl at 950 °C (red spectrum). The deconvolution of W 4f<sub>5/2</sub>, W 4f<sub>7/2</sub> and W 5p core levels and overall fit of the spectrum are reported as black dashed and a continuous line respectively. (b) The S 2p<sub>1/2</sub> and 2p<sub>3/2</sub> core levels for each of the two growth conditions are reported in the central panel. (c) W 4f<sub>5/2</sub>, W 4f<sub>7/2</sub> and W 5p core levels before (dashed line) and after transfer (continuous like) onto a new SiO<sub>2</sub>/Si substrate are compared showing the complete disappearance of the residual WO<sub>3</sub> components. The spectra were fit by Doniach-Sunjic function after subtracting a Shirley background (black dashed line).

The samples were further characterised for their electrical properties. Bottom-gated field effect transistors were prepared as seen in Figure 20. The FET transfer curve indicates accumulation-type n-channel transistor, where the drain current increases with applied gate bias after a threshold is crossed. Once the current-bias curve reaches linear range it can be described by  $I_d = \mu_n C_{ox} (W/L)((V_{gs} - V_{th})V_{ds})$ , where  $\mu_n$  is the electron field-effect mobility,  $C_{ox}$  is the oxide dielectric and  $V_{th}$  is the threshold voltage. As seen in Figure 20 a typical response curve for both the as grown as well as transferred samples of  $WS_2$  grown with  $H_2WO_4$  show an asymmetry around  $V_{ds} = 0$  V due to difference in the source and drain potentials. The Schottky barrier at the source is pinned by the gate, while the barrier at the drain diminishes proportionally to the drain bias and vice versa. The contacts however become more "Ohmic", when the bands bend more at the semiconductor/metal interface while the gate bias increase, leading to more significant

tunnelling current.

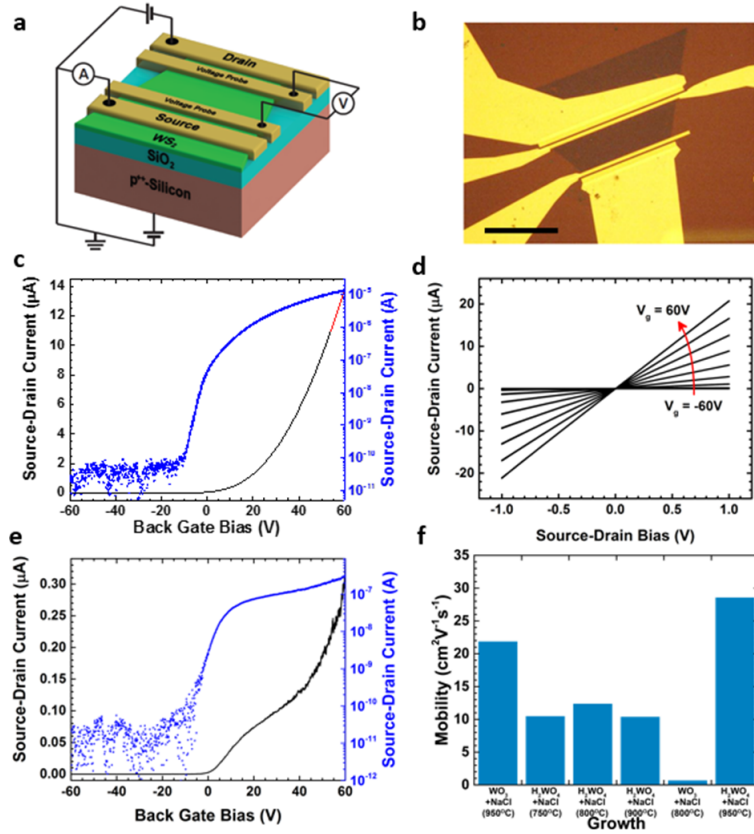


Figure 20: Electrical characteristics of monolayer WS<sub>2</sub>: (a) Schematic of the bottom-gated field effect transistors; (b) optical micrograph of the device (scale bar is 20μm); (c) FET transfer curve for the monolayer WS<sub>2</sub> grown using H<sub>2</sub>WO<sub>4</sub>+NaCl at 950 °C showing the highest mobility of 28 cm<sup>2</sup>/Vs (linear region of the transport graph marked with a red-dashed line); (d) Response curves at different gate biases for a WS<sub>2</sub> triangle grown using H<sub>2</sub>WO<sub>4</sub>+NaCl; (e) FET transfer curve for the monolayer WS<sub>2</sub> grown using WO<sub>3</sub>+NaCl at 800 °C; (f) electron mobilities of monolayer WS<sub>2</sub> grown using different conditions.

By looking at the linear regime of the transport graph (red-dashed line in Figure 20) the field-effect mobility can be calculated as  $\mu_n = C_{ox}^{-1}(d\sigma/dV_{gs})$ . The electron mobility calculated for WS<sub>2</sub> grown with H<sub>2</sub>WO<sub>4</sub>+NaCl is generally higher than that of WS<sub>2</sub> grown with WO<sub>3</sub> + NaCl (Figure 20) which further indicates higher crystal quality when using H<sub>2</sub>WO<sub>4</sub>. The monolayer WS<sub>2</sub> exhibits electron mobility of 28 cm<sup>2</sup>V<sup>-1</sup>s<sup>-1</sup>, the highest reported value for CVD grown WS<sub>2</sub> and transferred onto SiO<sub>2</sub> [32][27][12][63][59][31][61][1][30][22][7] and comparable to mechanically exfoliated WS<sub>2</sub> [56][24][13][25]. The highest mobilities were recorded in WS<sub>2</sub> grown at 950 °C, grown with either H<sub>2</sub>WO<sub>4</sub>+NaCl or WO<sub>3</sub>+NaCl,

which indicates a role of the growth temperature in improving the quality of the  $WS_2$ . As the temperature is lowered the difference between precursors becomes more pronounced in terms of the crystal quality. The  $H_2WO_4 + NaCl$  precursor system grown  $WS_2$  shows electron mobility of 10 to 20  $cm^2V^{-1}s^{-1}$  at temperatures of 750 °C and 850 °C. The electron mobilities of  $WS_2$  grown using  $WO_3 + NaCl$  are much lower,  $\sim 2 cm^2V^{-1}s^{-1}$  at 800 °C. Bilayer  $WS_2$  samples have overall greater electron mobility than their monolayer equivalent (between  $\sim 38 cm^2V^{-1}s^{-1}$  and  $52 cm^2V^{-1}s^{-1}$ ), similarly to the mechanically exfoliated flakes [43][25]. The electron mobility of bilayer  $WS_2$  ( $52 cm^2V^{-1}s^{-1}$ ) (Figure 22 and Figure 21) is also higher than that of other CVD grown  $WS_2$  as well as mechanically exfoliated onto  $SiO_2$  samples of  $WS_2$  reported [23][43][25]. The highest mobility has been obtained for bilayer system using  $WO_3 + NaCl$  indicating that the precursor choice is less important for electron mobility in such systems.

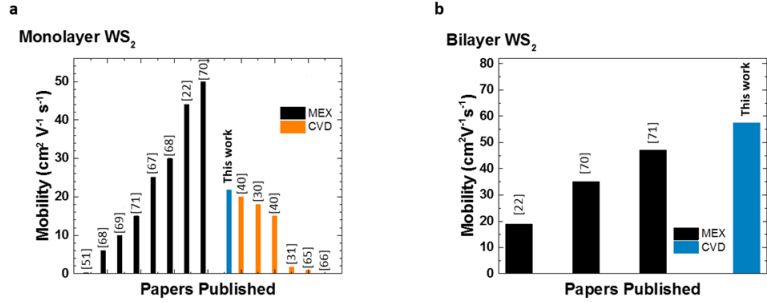


Figure 21: Comparison of our results with the literature of CVD grown material and mechanically exfoliated  $WS_2$  (MEX) : electron mobility for (a) monolayer  $WS_2$  and (b) bilayer  $WS_2$ . The histograms show our record values for both monolayer and bilayer amongst the best values reported for CVD grown  $WS_2$ .

## 2.3 Conclusions

In conclusion a synthesis route has been developed that allows for high quality monolayer and bilayer  $WS_2$  CVD growth. This quality is demonstrated by highest recorded electron FET mobility for both monolayer and bilayer CVD grown  $WS_2$  compared to the literature and comparable to that of mechanically exfoliated ones. Additionally the triangle flakes grown using  $H_2WO_4 + NaCl$  are much larger (up to  $\sim 200\text{--}300 \mu m$ ) compared to ones grown using standard  $WO_3$ . The CVD growth using  $H_2WO_4$  has also been demonstrated to work at lower temperatures, down to 750 °C compared to more commonly used 950 °C. Finally the PL of the  $WS_2$  grown using  $H_2WO_4$  is uniform throughout the flake and

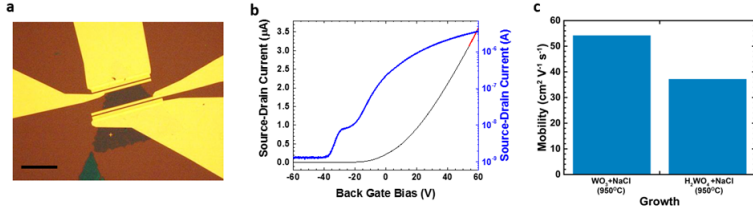


Figure 22: Electrical characteristics of bilayer WS<sub>2</sub>: (a) Optical micrograph of the device (scale bar is 30μm); (b) FET transfer curve for the bilayer WS<sub>2</sub> grown using WO<sub>3</sub>+NaCl at 950 °C showing the highest mobility of 52 cm<sup>2</sup>/Vs (linear region of the transport graph marked with a red-dashed line); (c) electron mobility of bilayer WS<sub>2</sub> grown by using different precursor systems.

has very FWHM (36 meV) which again points to high crystal quality and lack of defects in form of sulfur vacancies. These findings allow to develop further the TMDCs synthesis method of CVD and can potentially lead to industrially scalable synthesis of monolayer WS<sub>2</sub> or other TMDCs over large area.

## 3 WSe<sub>2</sub>

### 3.1 Introduction

*WSe<sub>2</sub>* is a TMDC material very similar to the *WS<sub>2</sub>*. The main difference is its bandgap which for monolayer is about 1.65 eV. This allows for potential application in the near infrared range. Its crystal structure is the same as the other TDMCs as outlined in 1.4. The electronic structure can be seen in Figure 23 and it is very similar to that of the *WS<sub>2</sub>*.

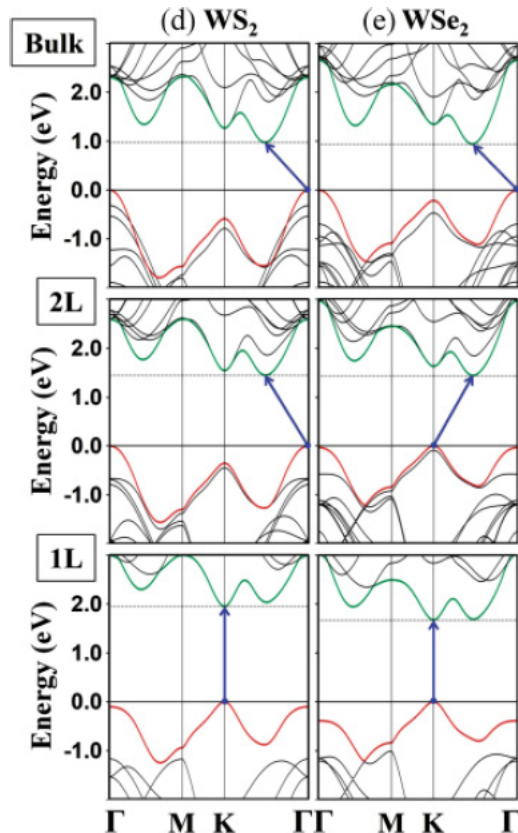
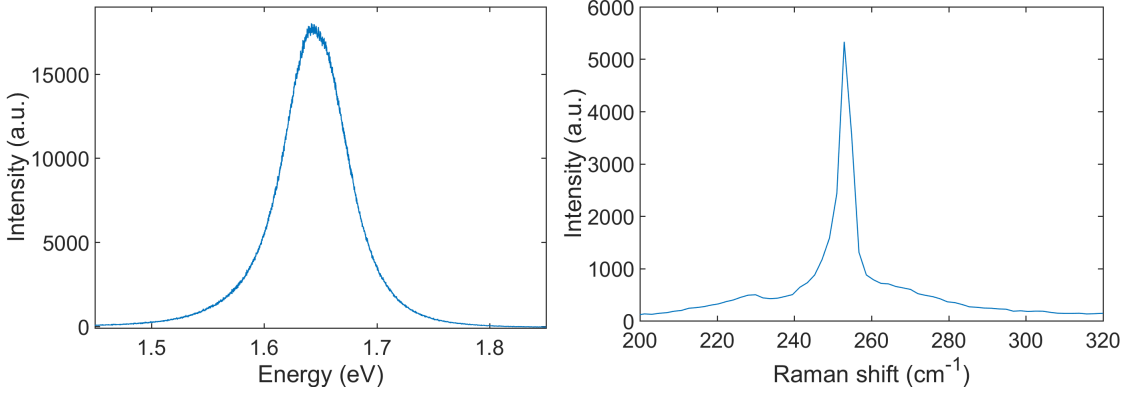


Figure 23: *WS<sub>2</sub>* and *WSe<sub>2</sub>* electronic band structure for 1, 2 and many layers (bulk)

### 3.2 Results

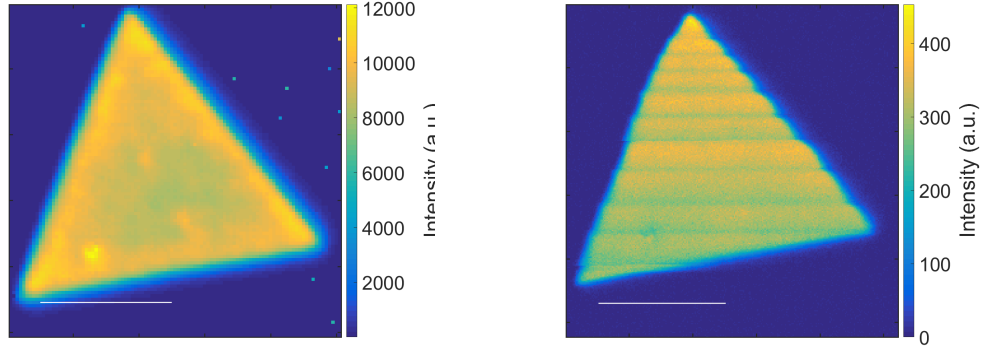
A typical PL and Raman spectrum can be seen in Figure 24. The PL peak is mostly symmetrical with little to no trion component as seen in *WS<sub>2</sub>* flakes. The peak is centred at around 1.645 eV with FWHM of 66 meV. The Raman peak around  $250\text{ cm}^{-1}$  is a convolution of 2 peaks, a  $E_{2g}^1$  and  $A_{1g}$  peaks.

A typical map of PL intensity of a *WSe<sub>2</sub>* sample can be seen in Figure 25a. The PL



(a) Typical PL spectrum from monolayer  $WSe_2$       (b) Typical Raman spectrum from monolayer  $WSe_2$

Figure 24: PL and Raman spectra from monolayer  $WSe_2$



(a) PL intensity      (b) Raman  $E_{2g}^1$  intensity

Figure 25: PL intensity and Raman  $E_{2g}^1$  intensity maps

intensity is homogeneous throughout the flake. It does not exhibit the trisecting pattern as seen in  $WS_2$  samples e.g. Figure 25a.

A comparison of PL peak positions and widths between different samples of WSe<sub>2</sub> can be seen in Figure 26.

By plotting the intensity and width of the PL peaks against the peak position as seen in Figure 27 certain patterns can be observed. The intensity is mostly grouped around maximum values and relatively narrowly spread across the position spectrum. The thick flakes show much more even distribution of intensity across the position, which combined with the wide distribution of positions results in a much more inhomogeneous sample. The width and positions are generally well grouped with flakes with smaller width having

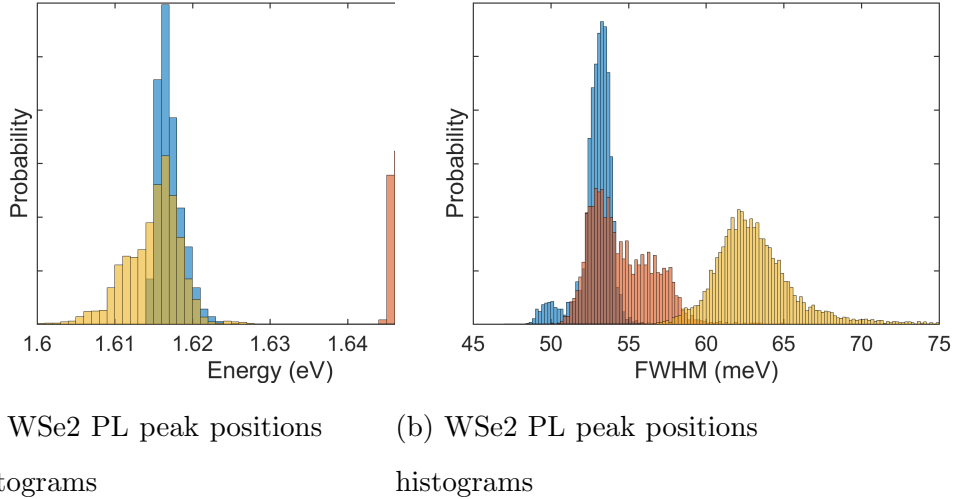


Figure 26: Comparison of PL peak positions and widths in different  $WSe_2$  samples

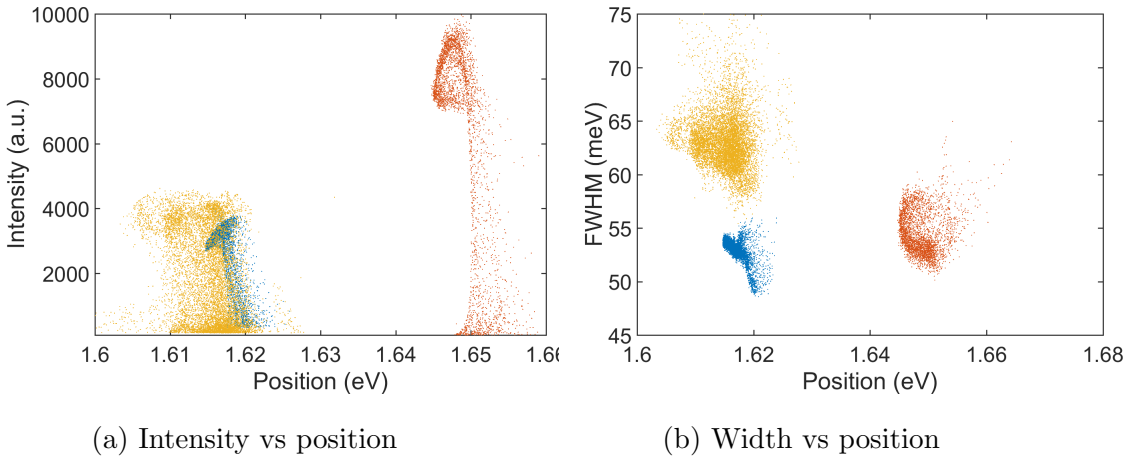


Figure 27: PL peak parameters distribution

more narrow distribution than those with greater width. Also few-layer flake shows a smaller peak width. Overall there is no obvious relation between position and width.

The Raman spectroscopy is a very useful characterisation technique for TMDCs. For most TMDCs it can be used to identify the number of layers or strain within the layer. However in the case of  $WSe_2$  the position of the  $E_{2g}^1$  and  $A_{1g}$  largely overlaps and therefore it is difficult to accurately determine the difference in their position. Because of that this method of identifying the number of layers cannot be employed easily. It is however still possible to examine the strain within the layers by noting the shift of the  $E_{2g}^1$  peak. A Raman  $E_{2g}^1$  peak position distribution from a representative sample can be seen in Figure 28. The strain can be then determined from the mean position of  $250.678 \pm 0.095 \text{ cm}^{-1}$

to be 2.44 % [8].

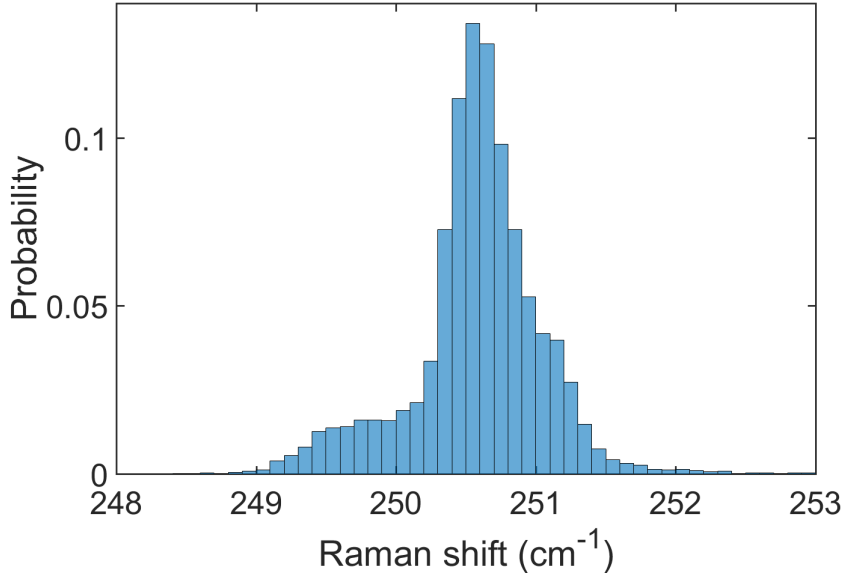


Figure 28: Histogram of Raman  $E_{2g}^1$  peak position from monolayer  $WSe_2$

The sample has been further characterised with XPS. Three areas were selected for measurements, one with thin, mono or double layer  $WSe_2$ , one with thick bulk  $WSe_2$  and one with no visible  $WSe_2$  flakes. The Figure 30 shows W4f core levels measured in those spots. The first area (Figure 30a), with thin flake shows one doublet at 32.08 eV and 34.23 eV and a second doublet at 35.33 eV and 37.68 eV. The first doublet corresponds to  $WSe_2$  while the second one can be attributed to  $WO_3$ . Since the spot size in the measurement covers both the flake as well as some surrounding substrate it is possible that the  $WO_3$  is located outside of the flake. Furthermore the background indicates that the emission from  $WS_2$  came from surface and therefore the  $WS_2$  flake is not contaminated with  $WO_3$ . The second area with thicker flakes (Figure 30b) shows similarly two doublets: one at 32.28 eV and 34.43 eV and a second one at 35.38 eV and 37.63 eV. Similarly to the thin area with thin flake we can ascribe the former to the  $WS_2$  and the latter to  $WO_3$ . There is a small shift of 0.2 eV between  $WS_2$  from the thin flake and  $WS_2$  from the thick flake. It is possible that XPS is sensitive to the number of layers in  $WSe_2$  and TMDCs in general since it is known that number of layers does modify the electronic structure of the material. The  $WO_3$  is found to be at the same position in both areas. The  $WO_3$  peak is also relatively weaker in the area with the thick flake than in the area with thin flake which could be a result of the thick flake having larger surface area than the thin flake and smaller presence of  $WO_3$  around the flake. Additionally and empty area (Figure 30c)

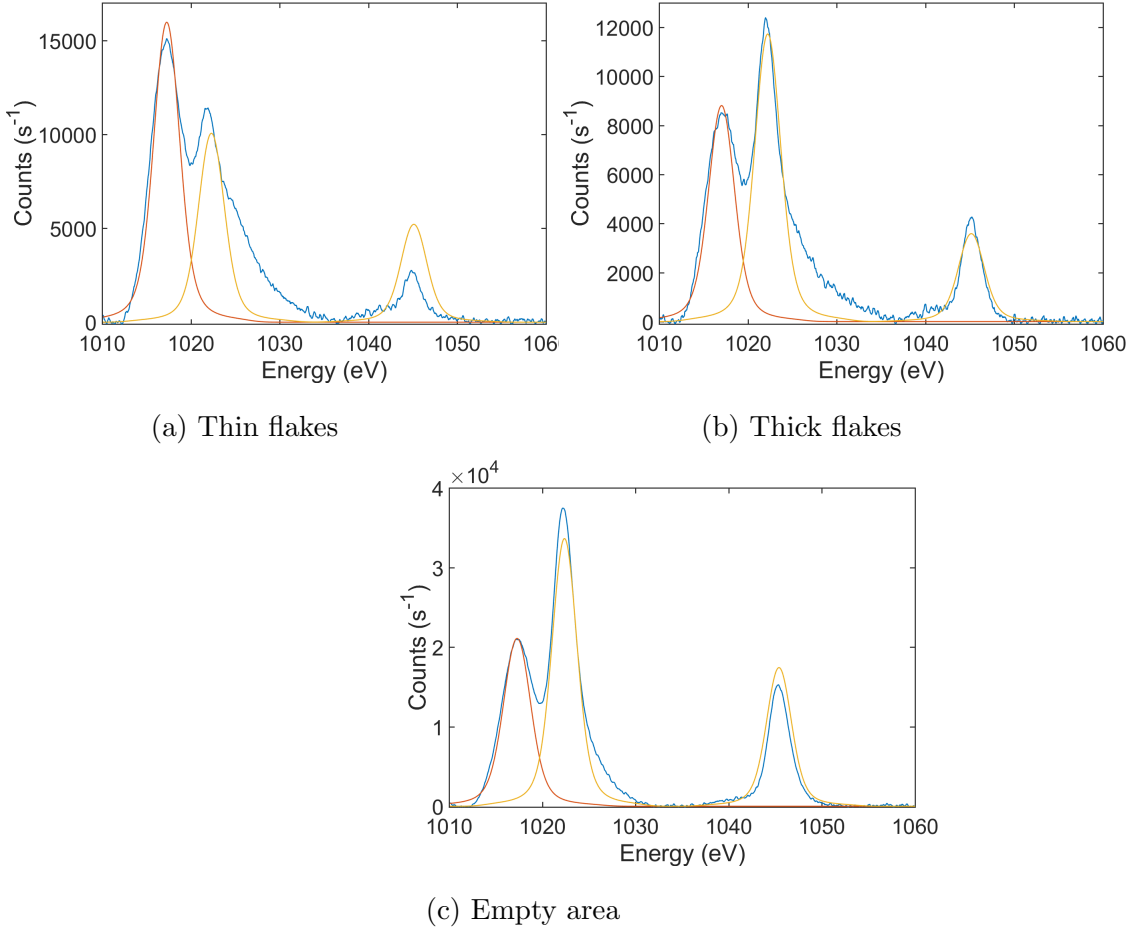


Figure 29: XPS spectra of Zn2p peaks in different areas of the sample

with no visible flakes have been measured. Similarly two doublets, one at 32.58 eV and 34.73 eV and a second one at 35.48 eV and 37.58 eV have been fitted and their presence can be again explained by presence of  $WS_2$  and  $WO_3$ . The  $WS_2$  peak is shifted in relation to that from the thin flake by 0.5 eV which could indicate presence of a highly defective  $WS_2$  or very small amounts of very bulk  $WS_2$ . The  $WS_2$  peak is also much weaker than that of the  $WO_3$  which is expected since no visible  $WS_2$  flakes were observed.

We can also look at Se3d core levels measured at the same locations. As seen in Figure 31a, taken from an area with the thin flake, we can fit it with one doublet corresponding to the presence of  $WS_2$  at 54.48 eV and 55.23 eV. Similarly in Figure 31b we can see Se3d peaks taken from area with the thick flake and can fit it with a doublet at 54.63 eV and 55.38 eV which also corresponds to the  $WS_2$ . Similar to the W4f levels there is a shift of 0.15 eV between those two flakes which can be explained by their thickness which changes the electronic structure. The Se3d levels measured in the reference empty area also can be fitted with a doublet at 54.53 eV and 55.33 eV which can be attributed to

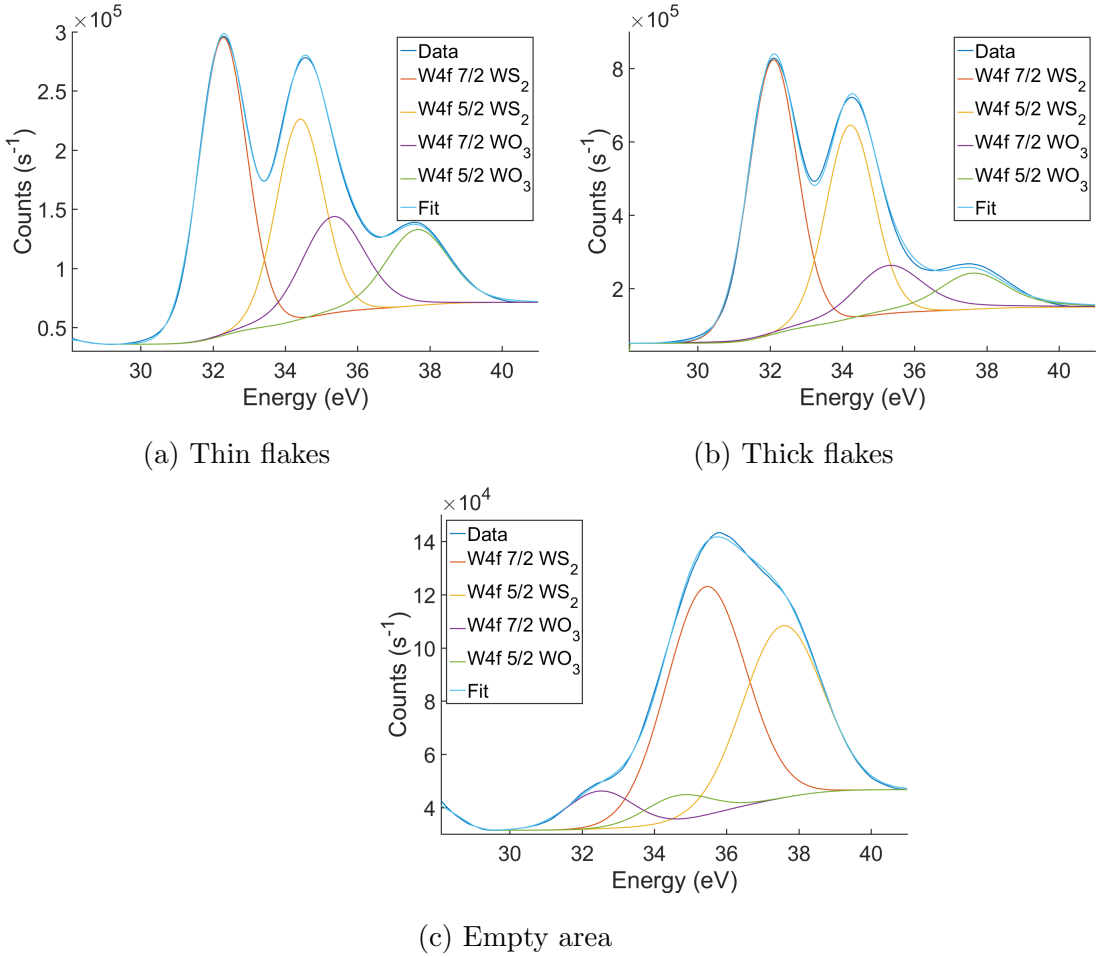


Figure 30: XPS spectra of W4f peaks in different areas of the sample

$WS_2$ . Similarly there is a shift of 0.05 eV from the peak associated with the thin flake, which is much smaller than the W4f peak shift. The Se3d peak from the empty area is about a magnitude weaker than that from either the thin or thick flake which is expected as no visible flake was observed. It does however indicate a non insignificant presence of  $WS_2$ , perhaps in the form of nuclei that never grew into proper flakes or flakes that shrunk or became etched and are highly defective and thinner than monolayer. The Se3d from the empty area also exhibits a steep background which indicates that the Se is covered with some layer, perhaps that of  $WO_3$ .

Finally the Zn2p levels were measured across the same areas. As seen in Figure ?? a doublet can be identified at

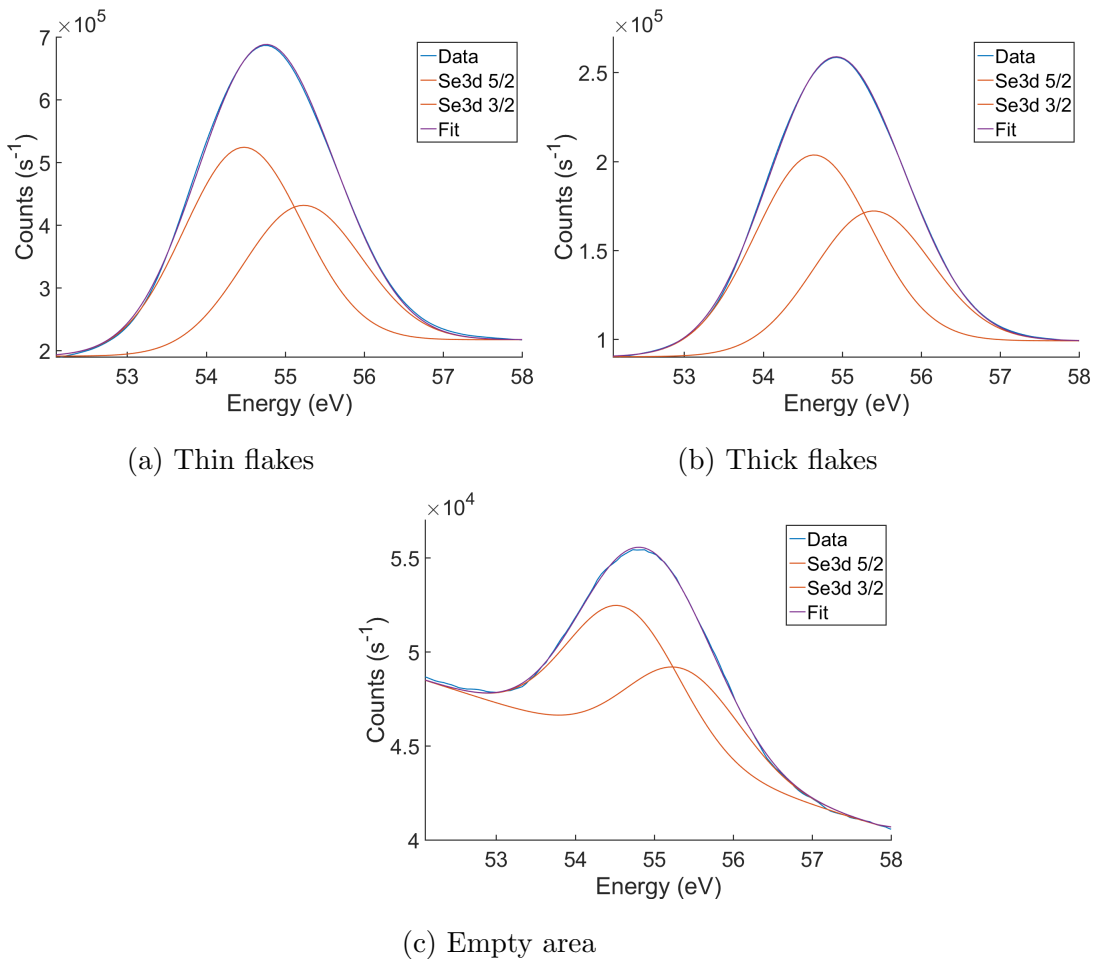


Figure 31: XPS spectra of Se3d peaks in different areas of the sample

## 4 Transfer

### 4.1 Introduction

The most common method of producing the TMDCs is CVD. During the CVD growth the process the substrate and the sample are heated to very high temperatures, up to 1000 °C. Because of that there is substantial thermal expansion in both substrate and sample. However due to difference in thermal expansion coefficient between those two elements there is potential build up of thermal strain. Additionally because the substrate, upon which the sample is grown, is heated to such high temperatures that it cannot be used for electrical measurements. More specifically the thermal expansion coefficients of  $WS_2$  and  $SiO_2$  are on the order of  $10^{-3}$  and  $10^{-7} K^{-1}$  respectively [19][?]. Therefore it is expected that during cooling down the  $WS_2$  will come under tension due to thermal expansion coefficient misalignment. Moreover in order to use TMDCs as components in devices different layers have to be arranged together either vertically or laterally. Due to aforementioned reasons there is a need to develop methods for transferring single layers of TDMCs from one substrate to another one. In this chapter a focus is put on transferring  $WS_2$  monolayer flakes from  $SiO_2/Si$  onto other surfaces.

### 4.2 Experimental

The most common method of transferring flakes synthesised via CVD method is a wet transfer method utilising as an intermediate substrate. In such procedure a thin layer of PMMA is first spun on top of the substrate. After drying the substrate is placed in a KOH aqueous solution (6% to 8%) heated to about 50 °C. As a result the thin layer of  $SiO_2$  on top of  $Si$  is dissolved leaving a PMMA with the sample attached to it floating on top of the solution. The PMMA is then rinsed in water several times and scooped up onto a new substrate. Next the sample is dried and annealed to ensure good adhesion and remove wrinkles and strain. Then the PMMA is removed with a solution of acetone and IPA at about 50 °C. Any remaining PMMA can be removed by annealing the sample at about 100 °C.

### 4.3 Results

A sample has been investigated using Raman and PL spectroscopy before and after transfer. In Figure 32 a comparison between samples before and after transfer can be seen in

PL spectra. The as grown sample shows mostly homogeneous PL intensity, position and FWHM across the sample with the exception of the edge and trisecting lines in the middle where the PL intensity is higher and lower accordingly. In the sample after transfer the PL intensity, position and FWHM is more randomly distributed across the flake and there is a distinct lack of edge enhancement or the presence of trisecting lines.

The position of the PL peak from the as grown sample is  $1.9765 \pm (9.8445 \times 10^{-4})$  eV, while the PL peak position from transferred sample  $1.9703 \pm (8.3518 \times 10^{-3})$  eV. Therefore the peak position is shifted by 6.2 meV after transfer while the relative standard deviation is about 8.5 times greater in the transferred sample than in the as grown sample. The FWHM in the as grown sample is  $36.3693 \pm 0.7982$  meV while in the transferred sample the FWHM is  $83.2706 \pm 6.7947$  meV. The FWHM then increases by 46.9013 meV while the relative standard deviation increases 3.726 times compared to the as grown sample.

The Raman  $E_{2g}^1$  peak position in the as grown sample is  $350.8681 \pm 0.2064$   $cm^{-1}$  while in the transferred sample is  $351.3407 \pm 0.2893$   $cm^{-1}$ . The relative uncertainty is therefore 1.3997 greater in the transferred sample. The position of the Raman  $A_{1g}$  peak in the as grown sample is  $418.6530 \pm 0.2829$   $cm^{-1}$  while in the transferred sample it is  $417.3195 \pm 0.4760$   $cm^{-1}$ . The relative uncertainty is therefore 1.6879 times greater in the transferred sample. The position difference between these two peaks is  $67.7862 \pm 0.2411$   $cm^{-1}$  in the as grown sample while it is  $66.0040 \pm 0.4757$   $cm^{-1}$  in the transferred sample. The relative uncertainty increases therefore by 2.0264 after the transfer. The intensity ratio between those peaks in the as grown sample is  $5.7471 \pm 0.6844$  and after transfer it is  $7.1609 \pm 0.8899$ . The relative uncertainty changes 1.5835 times after transfer.

It can be therefore seen that after transfer the relative uncertainty increases for every parameter of Raman and PL spectra maps. This indicates that the sample after the transfer is much less homogeneous. Because both the position of PL as well as the position of Raman peaks is affected by the strain the inhomogeneity can indicate a relaxation or build up of strain. Since the CVD growth method involves heating up the sample and the substrate to very high temperatures, up to  $850^\circ C$ , there is possibility of residual thermal strain after cooling down. Since the PMMA is much more flexible than the  $SiO_2$ , that the sample is grown on, the  $WS_2$  can relax before being placed on a new  $SiO_2$  substrate. On the other hand the water present in between the  $WS_2$  and PMMA can also be a source of strain. During the water evaporation the surface tension can induce local strain leading to high inhomogeneity. The PMMA can also have varying thickness and can swell to small degree therefore contracting in size during drying. Any or all of these effects can

potentially contribute to the variation in parameters observed.

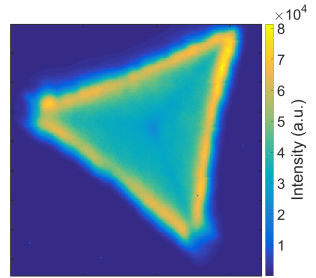
The average values of peak fitting parameters can be then compared between the two sample states to estimate the strain in the sample. The average position of  $E_{2g}^1 + 2LA$  peak changes from  $350.8601\text{ cm}^{-1}$  to  $351.3407\text{ cm}^{-1}$ , a  $0.4806\text{ cm}^{-1}$  difference. Since the position of this peak changes by  $-3.1\text{ cm}^{-1}/\%$  this indicates the change in strain of  $-0.155\%$ . The  $E_{2g}^1 + 2LA$  peak intensity change ( $\Delta I/I_0$ ) of  $23.15\%$  indicates a  $0.23\%$  change in strain. The average value of  $A_{1g}$  peak position changes from  $418.6530\text{ cm}^{-1}$  to  $417.3195\text{ cm}^{-1}$ , a difference of  $1.3335\text{ cm}^{-1}$ . This indicates then a strain of  $-4.445\%$ . The intensity change of  $A_{1g}$  peak of  $25.64\%$  corresponds to  $0.3344\%$  strain.

The PL peak position changes from  $1.9765\text{ eV}$  to  $1.9703$  which corresponds to change from about  $1\%$  to  $0.75\%$  strain, a  $-0.25\%$  change.

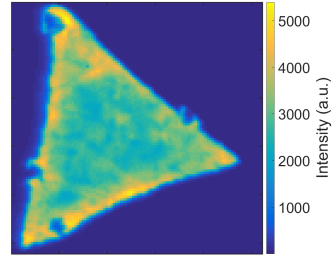
By comparing different average Raman and PL peaks fit parameters it is not clear to what extent the  $WS_2$  is strained before or after the transfer. Neither the direction nor the extent of strain can be estimated then in the sample overall. The difference in deviation of these values however indicates that the sample after transfer is less homogeneous than before. Therefore while it cannot be said that the sample strain changes on average as a whole, there is a change in strain across the sample. While the thermal strain should result in the sample as a whole being under tension due to thermal expansion and contraction other effects could still take place like aforementioned variation in water presence, inhomogeneity of PMMA layer thickness or folds in PMMA layer.

#### 4.4 Conclusions

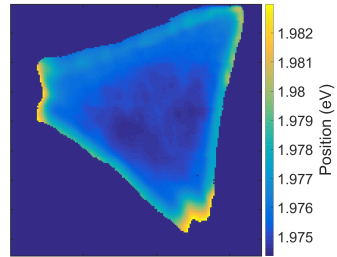
It is unclear to what extent the CVD grown  $WS_2$  sample is strained prior to transfer or after it. The difference in relative uncertainty of different fitting parameters of PL and Raman spectra however reveals that the sample becomes less homogeneous following the procedure. This could indicate that the strain becomes introduced during the transfer via a non uniform presence of water, non uniform thickness of PMMA layer, folds in the PMMA layer or presence of residue PMMA.



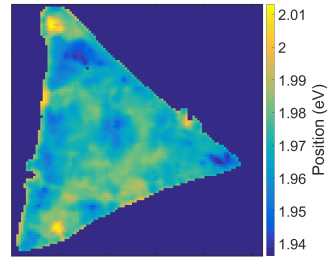
(a) PL Intensity map of as grown sample



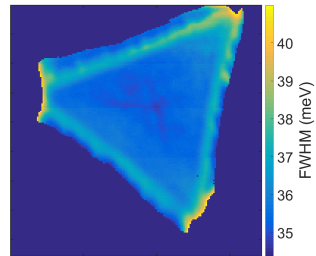
(b) PL Intensity map of transferred sample



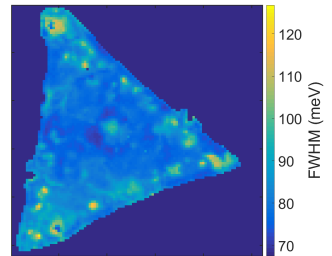
(c) PL Position map of as grown sample



(d) PL Position map of transferred sample

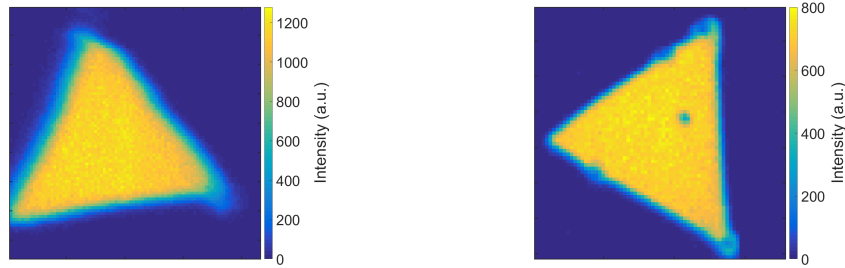


(e) PL FWHM map of as grown sample



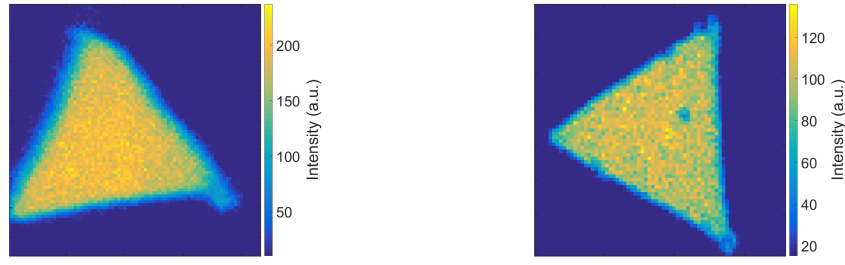
(f) PL FWHM map of transferred sample

Figure 32: PL spectra maps of samples before and after transfer



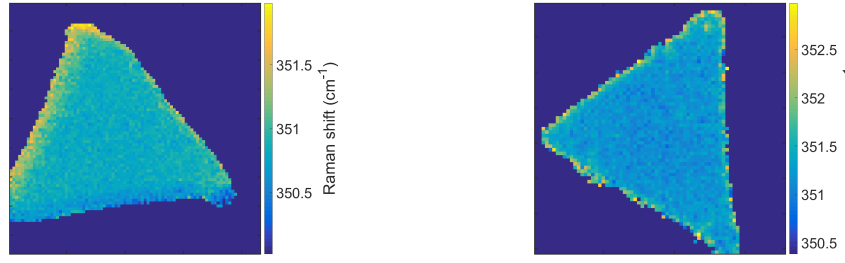
(a) Raman  $E_{2g}^1$  intensity map of as-grown sample

(b) Raman  $E_{2g}^1$  intensity map of transferred sample



(c) Raman  $A_{1g}$  intensity map of as-grown sample

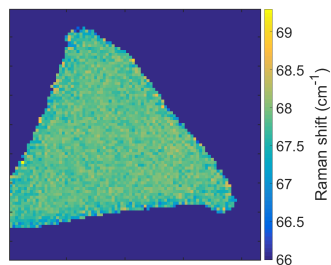
(d) Raman  $A_{1g}$  intensity map of transferred sample



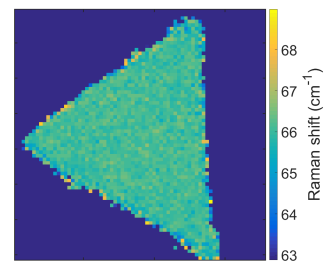
(e) Raman  $E_{2g}^1$  position map of as-grown sample

(f) Raman  $E_{2g}^1$  position map of transferred sample

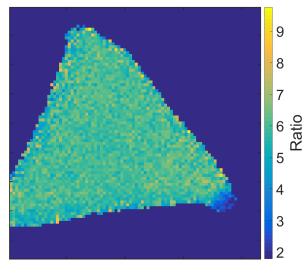
Figure 33: Raman spectra maps of samples before and after transfer



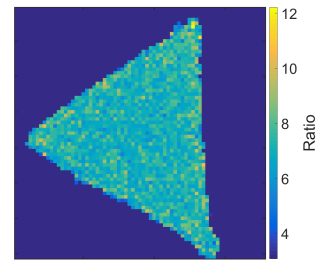
(a) Raman peak position difference map of as grown sample



(b) Raman peak position difference map of transferred sample



(c) Raman peaks ratio map of as grown sample



(d) Raman peaks ratio map of transferred sample

Figure 34: Raman spectra maps of samples before and after transfer

## 5 Low T PL

### 5.1 Introduction

As the temperature of the semiconductor goes down the number of charge carriers decreases. Because of this in  $WS_2$  the number of electrons is expected to be lower at low temperatures. Additionally as the temperature drops the peak broadening due to temperature effects i.e. Gaussian broadening decreases. At room temperature the thermal energy is equal to about 25 meV which limits the smallest possible width of the peak and therefore the resolution. Both of those effects should result in the peak at low temperatures to be overall weaker and more narrow than that at the room temperature. Additionally the lower electron density should result in lower population of trions. Due to lower temperature the electron and hole mobility should also decrease and cause the excitons to be more often trapped at defects sites also known as bound excitons.

### 5.2 Experimental

In order to perform the low temperature measurement the sample was placed in an environmental stage, Linkam THMS350V. The stage allows the sample to be cooled down to the temperatures of liquid nitrogen ( $LN_2$ ) and at pressures of down to  $10^{-3}$  mbar. The stage was then placed in a Renishaw Raman spectroscope chamber and the spectra were collected using 532nm green laser.

### 5.3 Results

The PL measurements were taken from the  $WS_2$  monolayer on  $Si/SiO_2$  sample at different conditions. As seen in Figure 35 the PL from has been measured in the same spot at lower pressure ( $2 \times 10^{-2}$ ) and different temperatures, room temperature and liquid nitrogen ( $LN_2$ ) temperature ( $-196^\circ C$ ). The PL from that spot at room temperature is centred at 1.957 eV and has FWHM of 44.3 meV. After lowering the temperature to that of  $LN_2$  i.e.  $-196^\circ C$  the PL measurement was taken again and the intensity of the peak was found to be about 0.81 that of the RT. Additionally the position of the PL at lower temperature was found to be 1.969 eV and the FWHM was 37.9 eV.

The PL spectra were then fitted with 2 peaks to resolve the trions and excitons. The results can be seen in Figure 36. Similarly the PL spectrum from room temperature has been fitted with two peaks. The intensity ratio between the exciton and trion in the low

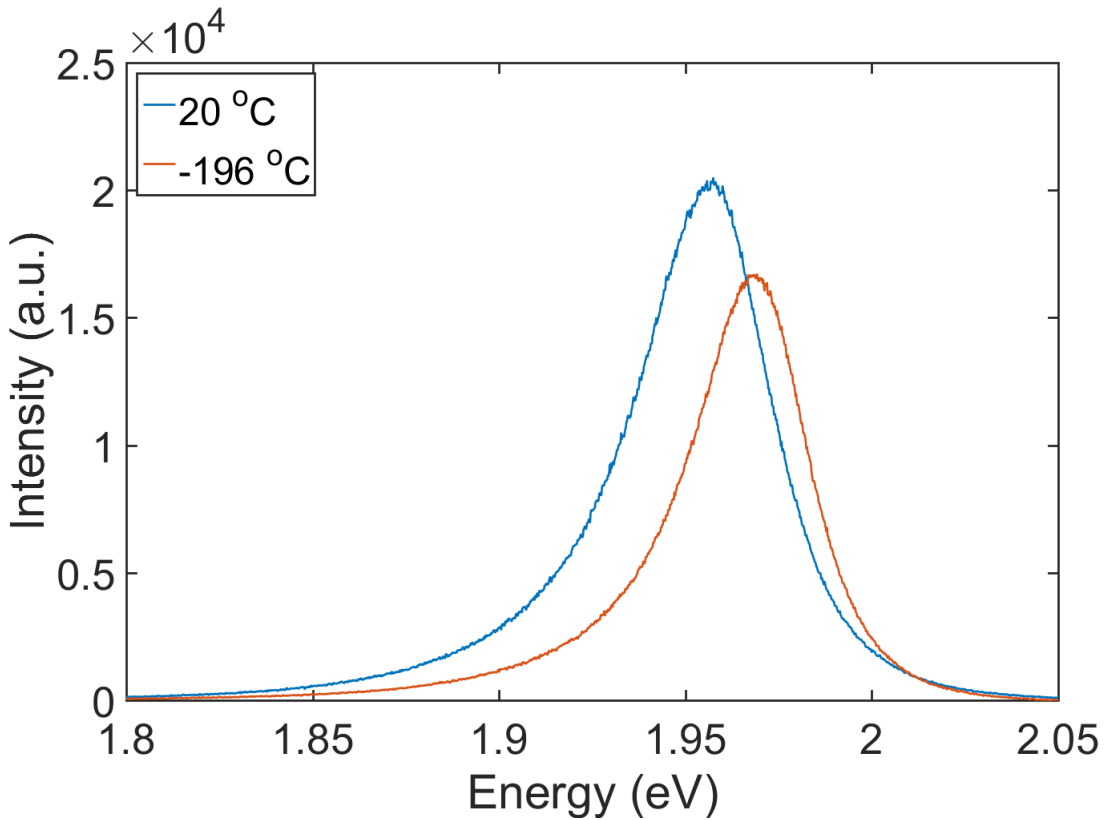


Figure 35: PL spectra of samples at room temperature and  $LN_2$  temperature at  $2 \times 10^{-2}$  mbar

temperature sample is about 4, while at the room temperature it is 3. The FWHM of the exciton peak also lowers from 36 meV to about 32 meV.

This indicates that indeed as the temperature is lowered the FWHM of the PL peak and especially the exciton component also lowers. However the difference between the FWHM at room temperature and low temperature is not as big as expected if temperature was the main contributor to the peak broadening. For room temperature a thermal energy contribution should be about 25 meV while at  $LN_2$  temperature (77 K) the contribution should be about half of that, i.e. 12 meV. The peak was fitted mostly with Gaussian lineshape (about 70%) and therefore the temperature should be a significant contributor to the peak width. It is possible that the laser heats up the sample during measurement since the thermal contact between the substrate and the cooled stage is weak. Additionally the glass window separating the stage and the room environment as well as the substrate itself can be covered in water droplets which could introduce refraction and therefore peak broadening.

Due to the low FWHM of the PL peaks a strong trion component can be observed as

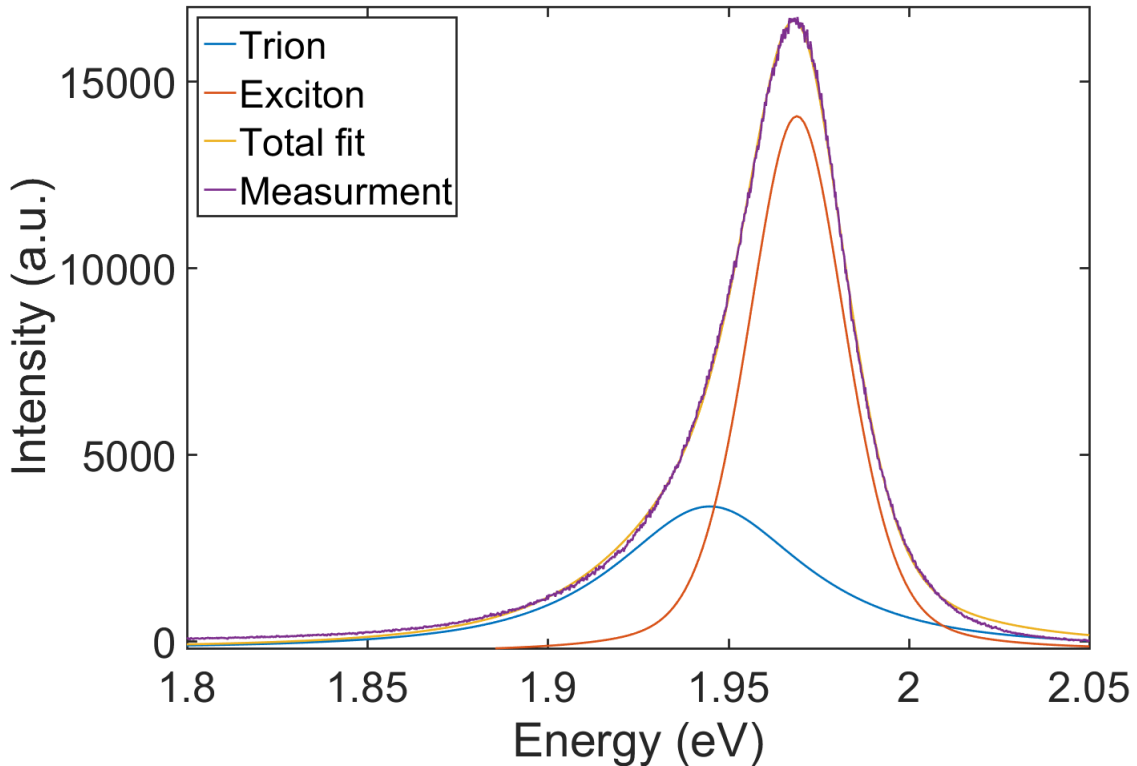


Figure 36: PL spectra at low temperature with trions and excitons components resolved

seen in Figure 37. While the lower temperature of the substrate can explain the small FWHM, the trion component is much stronger than in standard measurement environment. This could be caused by the low pressure which results in less oxygen and water molecules adsorbed at the defect sites. At standard conditions (1 atm) these species adsorb at the defect sites and attract electrons which as a result lowers the overall n-doping level of the material.

In order to check the influence of the pressure on the PL and potential effect of the adsorbed oxygen, nitrogen and water molecules measurement at different pressures was conducted. As seen in Figure 38 as the pressure is lowered by several orders of magnitude the PL peak is shifted to the red. The FWHM of the PL peak at the ambient pressure is about 41 meV while at lower pressure ( $1.5 \times 10^{-2}$  mbar) it is about 44 meV. The exciton to trion intensity ratio changes from 3.387 to 3.25 from the ambient pressure to low pressure. It therefore indicates that as the pressure is lowered the trion component becomes more prominent and the peak overall shifts to lower energies.

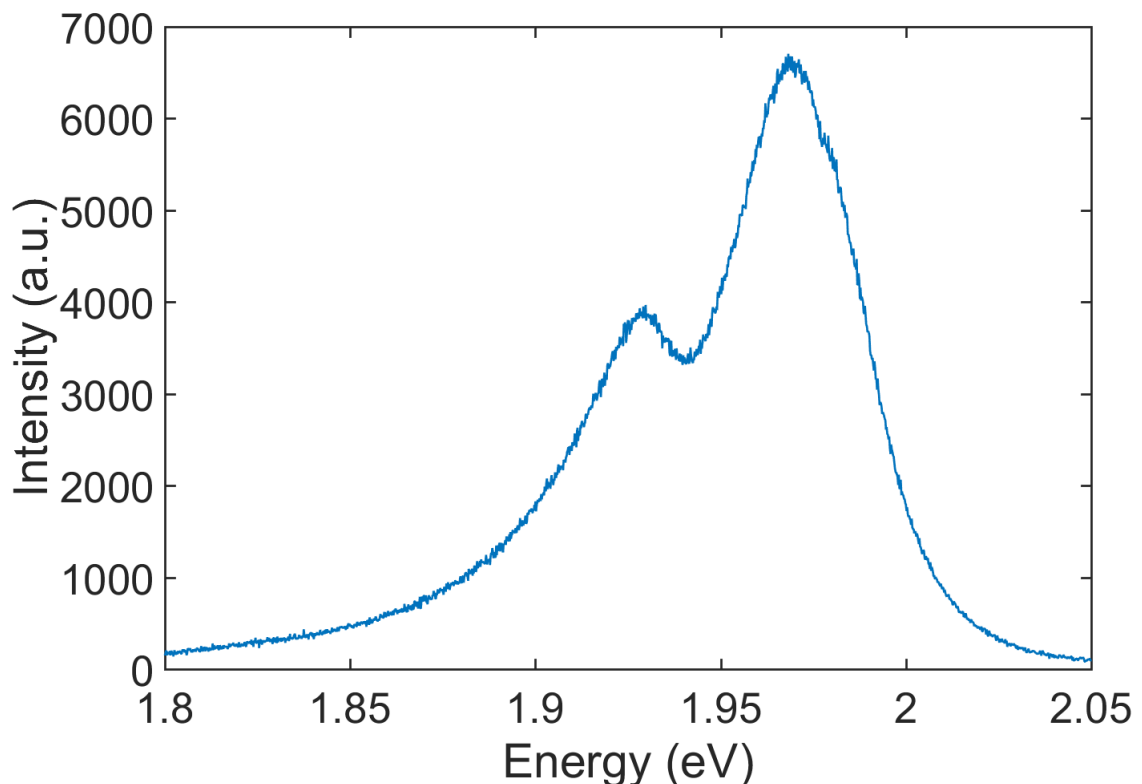


Figure 37: Low temperature PL spectrum with easily resolved strong trion component

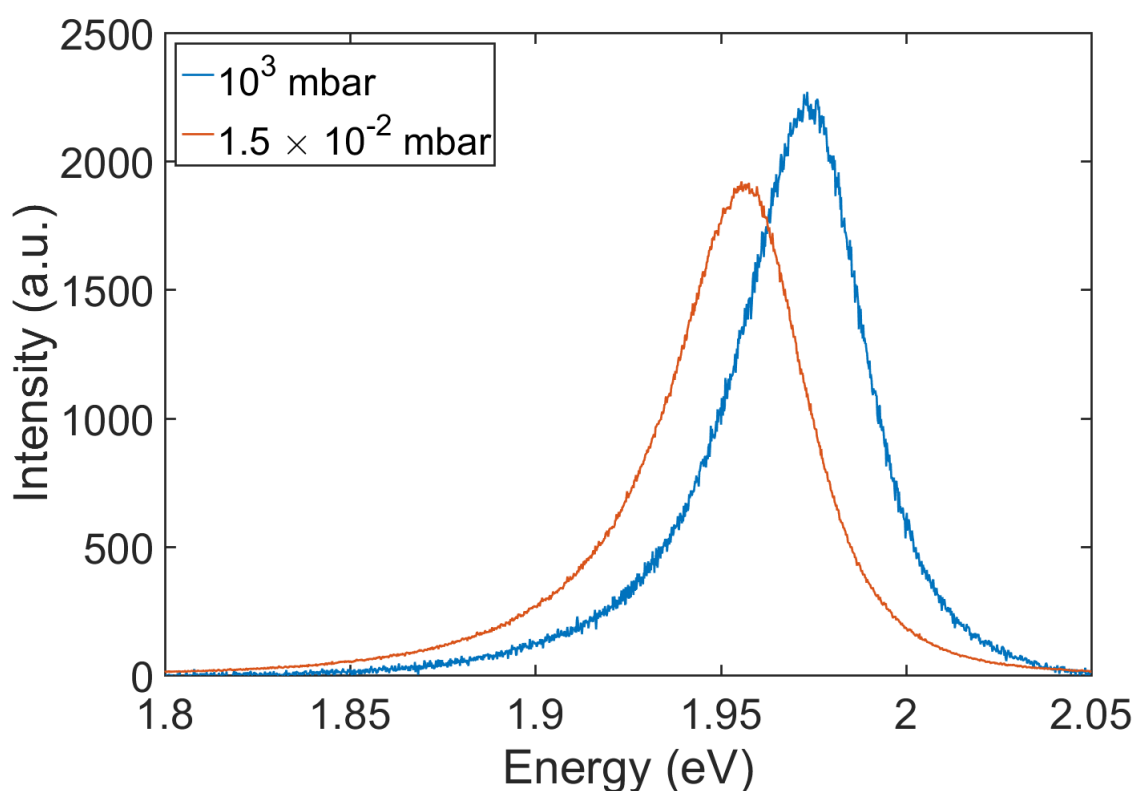


Figure 38: PL measurements at different atmospheric pressures

## **6 1T' $WSe_2$**

### **6.1 Introduction**

The

## 7 TMDC phases - review

### 7.1 Introduction

TMDCs, as mentioned in the introduction 1.4, are layered materials. In addition to the number of layers they can be also be primarily differentiated based on their structural polytype. The most common polytype seen in both mechanically exfoliated as well as CVD grown materials is the 2H phase. The name of it refers to the number of layers required to repeat the pattern as well as the symmetry, in this case the hexagonal symmetry.

## 8 Conclusions

## References

## Appendix

## Publications

F. Reale *et al.*, "High-Mobility and High-Optical Quality Atomically Thin  $WS_2$ " Scientific Reports, 2017 - submitted

F. M. Pesci *et al.*, "MoS<sub>2</sub>/WS<sub>2</sub> heterojunction for photoelectrochemical water oxidation", ACS Catalysis, 2017 - accepted

## Conferences

Graphene Week, 13-17 June, 2016. (Best poster)

UK Semiconductors, 14-15 July, 2017.

MRS Boston, 26 November - 1 December, 2017.

## References

- [1] Abdullah Alharbi and Davood Shahrjerdi. Electronic properties of monolayer tungsten disulfide grown by chemical vapor deposition. *Applied Physics Letters*, 109(19):193502, nov 2016.
- [2] M. Amani, D.-H. Lien, D. Kiriya, J. Xiao, A. Azcatl, J. Noh, S. R. Madhvapathy, R. Addou, S. KC, M. Dubey, K. Cho, R. M. Wallace, S.-C. Lee, J.-H. He, J. W. Ager, X. Zhang, E. Yablonovitch, and A. Javey. Near-unity photoluminescence quantum yield in MoS<sub>2</sub>. *Science*, 350(6264):1065–1068, nov 2015.

- [3] Marco Bernardi, Maurizia Palummo, and Jeffrey C. Grossman. Extraordinary sun-light absorption and one nanometer thick photovoltaics using two-dimensional monolayer materials. *Nano Letters*, 13(8):3664–3670, Aug 2013.
- [4] Claire J. Carmalt, Ivan P. Parkin, and Emily S. Peters. Atmospheric pressure chemical vapour deposition of WS<sub>2</sub> thin films on glass. *Polyhedron*, 22(11):1499–1505, jun 2003.
- [5] Mattia Cattelan, Brian Markman, Giacomo Lucchini, Pranab Kumar Das, Ivana Vobornik, Joshua Alexander Robinson, Stefano Agnoli, and Gaetano Granozzi. New strategy for the growth of complex heterostructures based on different 2d materials. *Chemistry of Materials*, 27(11):4105–4113, may 2015.
- [6] Chunxiao Cong, Jingzhi Shang, Xing Wu, Bingchen Cao, Namphung Peimyoo, Caiyu Qiu, Litao Sun, and Ting Yu. Synthesis and optical properties of large-area single-crystalline 2d semiconductor WS<sub>2</sub>monolayer from chemical vapor deposition. *Advanced Optical Materials*, 2(2):131–136, dec 2013.
- [7] Yang Cui, Run Xin, Zhihao Yu, Yiming Pan, Zhun-Yong Ong, Xiaoxu Wei, Junzhuan Wang, Haiyan Nan, Zhenhua Ni, Yun Wu, Tangsheng Chen, Yi Shi, Baigeng Wang, Gang Zhang, Yong-Wei Zhang, and Xinran Wang. High-performance monolayer WS<sub>2</sub>field-effect transistors on high- $\kappa$  dielectrics. *Advanced Materials*, 27(35):5230–5234, aug 2015.
- [8] A. M. Dadgar, D. Scullion, K. Kang, D. Esposito, E. H. Yang, I. P. Herman, M. A. Pimenta, E.-J. G. Santos, and A. N. Pasupathy. Strain engineering and raman spectroscopy of monolayer transition metal dichalcogenides. *Chemistry of Materials*, 30(15):5148–5155, jul 2018.
- [9] Sarah M. Eichfeld, Lorraine Hossain, Yu-Chuan Lin, Aleksander F. Piasecki, Benjamin Kupp, A. Glen Birdwell, Robert A. Burke, Ning Lu, Xin Peng, Jie Li, Angelica Azcatl, Stephen McDonnell, Robert M. Wallace, Moon J. Kim, Theresa S. Mayer, Joan M. Redwing, and Joshua A. Robinson. Highly scalable, atomically thin WSe<sub>2</sub> grown via metal–organic chemical vapor deposition. *ACS Nano*, 9(2):2080–2087, feb 2015.
- [10] Ana Laura Elías, Néstor Perea-López, Andrés Castro-Beltrán, Ayse Berkdemir, Ruitao Lv, Simin Feng, Aaron D. Long, Takuya Hayashi, Yoong Ahm Kim, Morinobu

- Endo, Humberto R. Gutiérrez, Nihar R. Pradhan, Luis Balicas, Thomas E. Mallouk, Florentino López-Urías, Humberto Terrones, and Mauricio Terrones. Controlled synthesis and transfer of large-area ws<sub>2</sub> sheets: From single layer to few layers. *ACS Nano*, 7(6):5235–5242, 2013. PMID: 23647141.
- [11] Qi Fu, Wenhui Wang, Lei Yang, Jian Huang, Jingyu Zhang, and Bin Xiang. Controllable synthesis of high quality monolayer WS<sub>2</sub> on a SiO<sub>2</sub>/si substrate by chemical vapor deposition. *RSC Advances*, 5(21):15795–15799, 2015.
- [12] Yang Gao, Zhibo Liu, Dong-Ming Sun, Le Huang, Lai-Peng Ma, Li-Chang Yin, Teng Ma, Zhiyong Zhang, Xiu-Liang Ma, Lian-Mao Peng, Hui-Ming Cheng, and Wencai Ren. Large-area synthesis of high-quality and uniform monolayer WS<sub>2</sub> on reusable au foils. *Nature Communications*, 6(1), oct 2015.
- [13] Thanasis Georgiou, Huafeng Yang, Rashid Jalil, James Chapman, Kostya S. Novoselov, and Artem Mishchenko. Electrical and optical characterization of atomically thin WS<sub>2</sub>. *Dalton Transactions*, 43(27):10388, 2014.
- [14] Yongji Gong, Junhao Lin, Xingli Wang, Gang Shi, Sidong Lei, Zhong Lin, Xiaolong Zou, Gonglan Ye, Robert Vajtai, Boris I. Yakobson, Humberto Terrones, Mauricio Terrones, Beng Kang Tay, Jun Lou, Sokrates T. Pantelides, Zheng Liu, Wu Zhou, and Pulickel M. Ajayan. Vertical and in-plane heterostructures from WS<sub>2</sub> /MoS<sub>2</sub> monolayers. *Nature Materials*, 13(12):1135–1142, sep 2014.
- [15] Yongji Gong, Zhong Lin, Gonglan Ye, Gang Shi, Simin Feng, Yu Lei, Ana Laura Elías, Nestor Perea-Lopez, Robert Vajtai, Humberto Terrones, Zheng Liu, Mauricio Terrones, and Pulickel M. Ajayan. Tellurium-assisted low-temperature synthesis of MoS<sub>2</sub> and WS<sub>2</sub> monolayers. *ACS Nano*, 9(12):11658–11666, nov 2015.
- [16] Humberto R. Gutiérrez, Nestor Perea-López, Ana Laura Elías, Ayse Berkdemir, Bei Wang, Ruitao Lv, Florentino López-Urías, Vincent H. Crespi, Humberto Terrones, and Mauricio Terrones. Extraordinary room-temperature photoluminescence in triangular ws<sub>2</sub> monolayers. *Nano Letters*, 13(8):3447–3454, dec 2013. PMID: 23194096.
- [17] Wolfgang K. Hofmann. Thin films of molybdenum and tungsten disulphides by metal organic chemical vapour deposition. *Journal of Materials Science*, 23(11):3981–3986, nov 1988.

- [18] Peng Hu, Jun Ye, Xuexia He, Kezhao Du, Keke K. Zhang, Xingzhi Wang, Qihua Xiong, Zheng Liu, Hui Jiang, and Christian Kloc. Control of radiative exciton recombination by charge transfer induced surface dipoles in MoS<sub>2</sub> and WS<sub>2</sub> monolayers. *Scientific Reports*, 6(1), apr 2016.
- [19] Xuan Hu, Poya Yasaee, Jacob Jokisaari, Serdar Öğüt, Amin Salehi-Khojin, and Robert F. Klie. Mapping thermal expansion coefficients in freestanding 2d materials at the nanometer scale. *Physical Review Letters*, 120(5), feb 2018.
- [20] Wang Yao Di Xiao Hualing Zeng, Junfeng Dai and Xiaodong Cui. Valley polarization in mos<sub>2</sub> monolayers by optical pumping. *Nature Nanotechnology*, 7(8):490–493, jun 2012.
- [21] Yeung Yu Hui, Xiaofei Liu, Wenjing Jie, Ngai Yui Chan, Jianhua Hao, Yu-Te Hsu, Lain-Jong Li, Wanlin Guo, and Shu Ping Lau. Exceptional tunability of band energy in a compressively strained trilayer MoS<sub>2</sub> sheet. *ACS Nano*, 7(8):7126–7131, jul 2013.
- [22] Aftab M. Hussain, Galo A. Torres Sevilla, Kelly R. Rader, and Muhammad M. Hussain. Chemical vapor deposition based tungsten disulfide (WS<sub>2</sub>) thin film transistor. In *2013 Saudi International Electronics, Communications and Photonics Conference*. IEEE, apr 2013.
- [23] M Waqas Iqbal, M Zahir Iqbal, M Farooq Khan, M Arslan Shehzad, Yongho Seo, Jong Hyun Park, Chanyong Hwang, and Jonghwa Eom. High-mobility and air-stable single-layer WS<sub>2</sub> field-effect transistors sandwiched between chemical vapor deposition-grown hexagonal BN films. *Scientific Reports*, 5(1), jun 2015.
- [24] Muhammad Waqas Iqbal, Muhammad Zahir Iqbal, Muhammad Farooq Khan, Muhammad Arshad Kamran, Abdul Majid, Thamer Alharbi, and Jonghwa Eom. Tailoring the electrical and photo-electrical properties of a WS<sub>2</sub> field effect transistor by selective n-type chemical doping. *RSC Advances*, 6(29):24675–24682, 2016.
- [25] Muhammad Waqas Iqbal, Muhammad Zahir Iqbal, Muhammad Farooq Khan, Muhammad Arslan Shehzad, Yongho Seo, and Jonghwa Eom. Deep-ultraviolet-light-driven reversible doping of WS<sub>2</sub> field-effect transistors. *Nanoscale*, 7(2):747–757, 2015.

- [26] Sanghyun Jo, Nicolas Ubrig, Helmuth Berger, Alexey B. Kuzmenko, and Alberto F. Morpurgo. Mono- and bilayer ws<sub>2</sub> light-emitting transistors. *Nano Letters*, 14(4):2019–2025, 2014. PMID: 24669957.
- [27] Kibum Kang, Saien Xie, Lujie Huang, Yimo Han, Pinshane Y. Huang, Kin Fai Mak, Cheol-Joo Kim, David Muller, and Jiwoong Park. High-mobility three-atom-thick semiconducting films with wafer-scale homogeneity. *Nature*, 520(7549):656–660, apr 2015.
- [28] Kyung Nam Kang, Kyle Godin, and Eui-Hyeok Yang. The growth scale and kinetics of WS<sub>2</sub> monolayers under varying h<sub>2</sub> concentration. *Scientific Reports*, 5(1), aug 2015.
- [29] A. Kuc, N. Zibouche, and T. Heine. Influence of quantum confinement on the electronic structure of the transition metal sulfide *ts*<sub>2</sub>. *Phys. Rev. B*, 83(24):245213, Jun 2011.
- [30] Changyong Lan, Chun Li, Yi Yin, and Yong Liu. Large-area synthesis of monolayer WS<sub>2</sub>and its ambient-sensitive photo-detecting performance. *Nanoscale*, 7(14):5974–5980, 2015.
- [31] Yi-Hsien Lee, Lili Yu, Han Wang, Wenjing Fang, Xi Ling, Yumeng Shi, Cheng-Te Lin, Jing-Kai Huang, Mu-Tung Chang, Chia-Seng Chang, Mildred Dresselhaus, Tomas Palacios, Lain-Jong Li, and Jing Kong. Synthesis and transfer of single-layer transition metal disulfides on diverse surfaces. *Nano Letters*, 13(4):1852–1857, mar 2013.
- [32] Shisheng Li, Shunfeng Wang, Dai-Ming Tang, Weijie Zhao, Huilong Xu, Leiqiang Chu, Yoshio Bando, Dmitri Golberg, and Goki Eda. Halide-assisted atmospheric pressure growth of large WSe<sub>2</sub> and WS<sub>2</sub> monolayer crystals. *Applied Materials Today*, 1(1):60–66, nov 2015.
- [33] Tianshu Li and Giulia Galli. Electronic properties of mos<sub>2</sub> nanoparticles. *The Journal of Physical Chemistry C*, 111(44):16192–16196, nov 2007.
- [34] Yilei Li, Yi Rao, Kin Fai Mak, Yumeng You, Shuyuan Wang, Cory R. Dean, and Tony F. Heinz. Probing symmetry properties of few-layer mos<sub>2</sub> and h-bn by optical second-harmonic generation. *Nano Letters*, 13(7):3329–3333, jun 2013. PMID: 23718906.

- [35] Liangxu Lin, Yaxian Xu, Shaowei Zhang, Ian M. Ross, Albert C. M. Ong, and Dan A. Allwood. Fabrication of luminescent monolayered tungsten dichalcogenides quantum dots with giant spin-valley coupling. *ACS Nano*, 7(9):8214–8223, 2013. PMID: 23968363.
- [36] Hongwei Liu, Junpeng Lu, Kenneth Ho, Zhenliang Hu, Zhiya Dang, Alexandra Carvalho, Hui Ru Tan, Eng Soon Tok, and Chorng Haur Sow. Fluorescence concentric triangles: A case of chemical heterogeneity in WS<sub>2</sub> atomic monolayer. *Nano Letters*, 16(9):5559–5567, aug 2016.
- [37] Zheng Liu, Matin Amani, Sina Najmaei, Quan Xu, Xiaolong Zou, Wu Zhou, Ting Yu, Caiyu Qiu, A. Glen Birdwell, Frank J. Crowne, Robert Vajtai, Boris I. Yakobson, Zhenhai Xia, Madan Dubey, Pulickel M. Ajayan, and Jun Lou. Strain and structure heterogeneity in MoS<sub>2</sub> atomic layers grown by chemical vapour deposition. *Nature Communications*, 5(1), nov 2014.
- [38] He Keliang Lee Changgu Lee Gwan Hyoung Hone James Heinz Tony F. Mak, Kin Fai and Jie Shan. Tightly bound trions in monolayer. *Nature Materials*, 12(3):207–211, dec 2013.
- [39] He Keliang Shan Jie Mak, Kin Fai and Tony F. Heinz. Control of valley polarization in monolayer mos<sub>2</sub> by optical helicity. *Nature Nanotechnology*, 7(8):494–498, jun 2012.
- [40] Kin Fai Mak, Changgu Lee, James Hone, Jie Shan, and Tony F. Heinz. Atomically thin mos<sub>2</sub>: A new direct-gap semiconductor. *Phys. Rev. Lett.*, 105(13):136805, Sep 2010.
- [41] H. Martinez, A. Benayad, D. Gonbeau, P. Vinatier, B. Pecquenard, and A. Levasseur. Influence of the cation nature of high sulfur content oxysulfide thin films MOySz (m=w, ti) studied by XPS. *Applied Surface Science*, 236(1-4):377–386, sep 2004.
- [42] Mitsuhiro Okada, Takumi Sawazaki, Kenji Watanabe, Takashi Taniguchi, Hiroki Hibino, Hisanori Shinohara, and Ryo Kitaura. Direct chemical vapor deposition growth of ws<sub>2</sub> atomic layers on hexagonal boron nitride. *ACS Nano*, 8(8):8273–8277, 2014. PMID: 25093606.

- [43] Dmitry Ovchinnikov, Adrien Allain, Ying-Sheng Huang, Dumitru Dumcenco, and Andras Kis. Electrical transport properties of single-layer WS<sub>2</sub>. *ACS Nano*, 8(8):8174–8181, jul 2014.
- [44] Namphung Peimyoo, Jingzhi Shang, Chunxiao Cong, Xiaonan Shen, Xiangyang Wu, Edwin K. L. Yeow, and Ting Yu. Nonblinking, intense two-dimensional light emitter: Monolayer ws<sub>2</sub> triangles. *ACS Nano*, 7(12):10985–10994, 2013. PMID: 24266716.
- [45] Namphung Peimyoo, Weihuang Yang, Jingzhi Shang, Xiaonan Shen, Yanlong Wang, and Ting Yu. Chemically driven tunable light emission of charged and neutral excitons in monolayer WS<sub>2</sub>. *ACS Nano*, 8(11):11320–11329, oct 2014.
- [46] Filip A. Rasmussen and Kristian S. Thygesen. Computational 2d materials database: Electronic structure of transition-metal dichalcogenides and oxides. *The Journal of Physical Chemistry C*, 119(23):13169–13183, jun 2015.
- [47] Youmin Rong, Ye Fan, Ai Leen Koh, Alex W. Robertson, Kuang He, Shanshan Wang, Haijie Tan, Robert Sinclair, and Jamie H. Warner. Controlling sulphur precursor addition for large single crystal domains of WS<sub>2</sub>. *Nanoscale*, 6(20):12096–12103, sep 2014.
- [48] Jingzhi Shang, Xiaonan Shen, Chunxiao Cong, Namphung Peimyoo, Bingchen Cao, Mustafa Eginligil, and Ting Yu. Observation of excitonic fine structure in a 2d transition-metal dichalcogenide semiconductor. *ACS Nano*, 9(1):647–655, 2015. PMID: 25560634.
- [49] Andrea Splendiani, Liang Sun, Yuanbo Zhang, Tianshu Li, Jonghwan Kim, Chi-Yung Chim, Giulia Galli, and Feng Wang. Emerging photoluminescence in monolayer mos<sub>2</sub>. *Nano Letters*, 10(4):1271–1275, apr 2010. PMID: 20229981.
- [50] Xiaona Liu Pingheng Tan Tengfei Yan, Xiaofen Qiao and Xinhui Zhang. Photoluminescence properties and exciton dynamics in monolayer wse<sub>2</sub>. *Applied Physics Letters*, 105(10):101901, sep 2014.
- [51] Sefaattin Tongay, Joonki Suh, Can Ataca, Wen Fan, Alexander Luce, Jeong Seuk Kang, Jonathan Liu, Changhyun Ko, Rajamani Raghunathanan, Jian Zhou, Frank Ogletree, Jingbo Li, Jeffrey C. Grossman, and Junqiao Wu. Defects activated photoluminescence in two-dimensional semiconductors: interplay between bound, charged and free excitons. *Scientific Reports*, 3(1), sep 2013.

- [52] Qing Hua Wang, Kourosh Kalantar-Zadeh, Andras Kis, Jonathan N. Coleman, and Michael S. Strano. Electronics and optoelectronics of two-dimensional transition metal dichalcogenides. *Nature Nanotechnology*, 7:699 EP –, Nov 2012. Review Article.
- [53] Kiran Kumar Amara Jing Ren Pang Minglin Toh Xin Zhang Christian Kloc Ping Heng Tane Weijie Zhao, Zohreh Ghorannevis and Goki Eda. Lattice dynamics in mono- and few-layer sheets of  $ws_2$  and  $wse_2$ . *Nanoscale*, 5(20):9677-9683, August 2013.
- [54] J.A. Wilson and A.D. Yoffe. The transition metal dichalcogenides discussion and interpretation of the observed optical, electrical and structural properties. *Advances in Physics*, 18(73):193–335, may 1969.
- [55] F. Withers, O. Del Pozo-Zamudio, A. Mishchenko, A. P. Rooney, A. Gholinia, K. Watanabe, T. Taniguchi, S. J. Haigh, A. K. Geim, A. I. Tartakovskii, and K. S. Novoselov. Light-emitting diodes by band-structure engineering in van der waals heterostructures. *Nature Materials*, 14(3):301–306, feb 2015.
- [56] Freddie Withers, Thomas Hardisty Bointon, David Christopher Hudson, Monica Felicia Craciun, and Saverio Russo. Electron transport of WS<sub>2</sub> transistors in a hexagonal boron nitride dielectric environment. *Scientific Reports*, 4(1), may 2014.
- [57] Ryan J. Wu, Michael L. Odlyzko, and K. Andre Mkhoyan. Determining the thickness of atomically thin MoS<sub>2</sub> and WS<sub>2</sub> in the TEM. *Ultramicroscopy*, 147:8–20, dec 2014.
- [58] Di Xiao, Gui-Bin Liu, Wanxiang Feng, Xiaodong Xu, and Wang Yao. Coupled spin and valley physics in monolayers of  $mos_2$  and other group-vi dichalcogenides. *Phys. Rev. Lett.*, 108(19):196802, May 2012.
- [59] Zai-Quan Xu, Yupeng Zhang, Shenghuang Lin, Changxi Zheng, Yu Lin Zhong, Xue Xia, Zhipeng Li, Ponraj Joice Sophia, Michael S. Fuhrer, Yi-Bing Cheng, and Qiao-liang Bao. Synthesis and transfer of large-area monolayer ws<sub>2</sub> crystals: Moving toward the recyclable use of sapphire substrates. *ACS Nano*, 9(6):6178–6187, 2015. PMID: 25961515.
- [60] Long Yuan and Libai Huang. Exciton dynamics and annihilation in WS<sub>2</sub> 2d semiconductors. *Nanoscale*, 7(16):7402–7408, 2015.

- [61] Seok Joon Yun, Sang Hoon Chae, Hyun Kim, Jin Cheol Park, Ji-Hoon Park, Gang Hee Han, Joo Song Lee, Soo Min Kim, Hye Min Oh, Jinbong Seok, Mun Seok Jeong, Ki Kang Kim, and Young Hee Lee. Synthesis of centimeter-scale monolayer tungsten disulfide film on gold foils. *ACS Nano*, 9(5):5510–5519, apr 2015.
- [62] Longhui Zeng, Lili Tao, Chunyin Tang, Bo Zhou, Hui Long, Yang Chai, Shu Ping Lau, and Yuen Hong Tsang. High-responsivity UV-vis photodetector based on transferable WS<sub>2</sub> film deposited by magnetron sputtering. *Scientific Reports*, 6(1), jan 2016.
- [63] Yu Zhang, Yanfeng Zhang, Qingqing Ji, Jing Ju, Hongtao Yuan, Jianping Shi, Teng Gao, Donglin Ma, Mengxi Liu, Yubin Chen, Xiuju Song, Harold Y. Hwang, Yi Cui, and Zhongfan Liu. Controlled growth of high-quality monolayer ws<sub>2</sub> layers on sapphire and imaging its grain boundary. *ACS Nano*, 7(10):8963–8971, 2013. PMID: 24047054.
- [64] Weijie Zhao, Zohreh Ghorannevis, Leiqiang Chu, Minglin Toh, Christian Kloc, Ping-Heng Tan, and Goki Eda. Evolution of electronic structure in atomically thin sheets of ws<sub>2</sub> and wse<sub>2</sub>. *ACS Nano*, 7(1):791–797, dec 2013. PMID: 23256505.
- [65] Z. Y. Zhu, Y. C. Cheng, and U. Schwingenschlögl. Giant spin-orbit-induced spin splitting in two-dimensional transition-metal dichalcogenide semiconductors. *Phys. Rev. B*, 84(15):153402, Oct 2011.